

Distributed large-scale joint non-uniform UAV formation path planning based on global optimal guidance

Gang Hu^{a,b,*}, Peidong He^a, Guo Wei^c

^a Department of Applied Mathematics, Xi'an University of Technology, Xi'an 710054, PR China

^b School of Computer Science and Engineering, Xi'an University of Technology, Xi'an 710048, PR China

^c University of North Carolina at Pembroke, Pembroke, NC 28372, USA



ARTICLE INFO

Keywords:

Path planning method
UAV formation
System fault-tolerant control strategies
Ablation experiments

ABSTRACT

In the military field, the utilization of unmanned aerial vehicle (UAV) formations to carry out saturation attacks on enemy forces is the development trend of future war. Traditional path planning algorithms have the disadvantages of poor real-time performance, poor flexibility, poor scalability, and weak anti-jamming ability, which make these algorithms difficult to apply in the control of large-scale joint non-uniform military UAV formations. This paper proposes a path-planning method for large-scale, low-cost military UAVs, it addresses three key aspects: system design, path-planning algorithms, and UAV safety guarantee. In system design, we implement a distributed formation control system. In this setup, individual agents can perform flight tasks independently using autonomous algorithms without needing to communicate with a central control center. In path planning algorithms, we quantify the four interactions of UAVs and combine them with the linear separation force strategy to construct a set of behavior-based formation coordination control methods through a reasonable interaction combination method. By adding guided paths, based on the integration of behavior-based formation coordination control methods, this paper retains the advantages of global path planning algorithms, such as high success rate, and local path planning algorithms, such as real-time performance. By designing a distributed formation control system with strong robustness and incorporating an escape mechanism, the system benefits from both passive and active fault-tolerant control strategies. This significantly enhances the overall stability of the system. Ablation experiments demonstrate that the components of the formation control system proposed in this paper are reasonable. Simulation experiments indicate that the distributed large-scale joint non-uniform UAV formation real-time path planning method is secure, stable, adaptable to various planning environments, and exhibits a fast convergence speed for the formation. Additionally, it is scalable, flexible, and suitable for application in large-scale clusters, among other benefits.

1. Introduction

In recent years, with the development of communication and automation technologies, with the flexibility, economies of scale, scalability, and mission execution efficiency of UAVs [1,2], they have been widely used in various fields. Sadi et al. proposed a multivariate system control architecture for UAVs that reduces the control performance and efficiency of UAV control systems in

* Corresponding author.

E-mail address: hugang@xaut.edu.cn (G. Hu).

mangrove ecosystems with wind disturbances [3]. Wen proposed a UAV control system for finding maritime search and rescue targets, which can automatically assign search tasks to individual UAVs in a formation [4]. Xu proposed a UAV route control system, which can reduce the deviation of the actual route from the planned route and improve the control accuracy [5]. UAVs have been used in scenarios such as fire scenario analysis [6], assessing water quality parameters [7], leading sand restoration [8], sustainable bio culture [9], airborne particulate matter concentration measurements [10], railroad infrastructure monitoring [11], and mine surface monitoring [12].

UAVs can be categorized into fixed-wing UAVs and multi-rotor UAVs based on their power source. Fixed-wing UAVs are known for their fast movement and large payload capacity. However, they face challenges when performing self-organized missions for several reasons. They cannot execute hovering and vertical take-off commands during mission execution, their horizontal turning and pitch angle are restricted during flight, and their aerodynamic parameters are influenced by their flight speed [13]. Compared to fixed-wing UAVs, multi-rotor UAVs rely on multiple rotating propeller sets to provide power. They are characterized by their small size, rich functionality, and simple handling, which has resulted in their increased prevalence.

Given the inherent limitations of a single UAV payload, using a multi-UAV formation to enhance mission efficiency has become a prevalent strategy during UAV operations. This approach is well-documented in the literature, with numerous studies attesting to its efficacy in improving mission success rates [14,15]. Wang et al. emphasized that when UAVs fly in a well-organized formation, the overall flight drag and energy loss are greatly reduced, and the overall load capacity and range of the formation are effectively enhanced [16]. This reduction occurs because the UAVs situated at the rear of the formation benefit from an improved lift-to-drag ratio. By connecting to a local network, multiple UAVs with varying performances and capabilities can be organized into a single task execution group. This collaborative approach to mission execution has become an essential trend in development [17]. Utilizing joint non-uniform formations for mission execution is a key research direction for the future [18].

Heterogeneous UAVs offer flexibility and cost reduction for system designers but pose challenges in mission planning. Automatic path planning for multiple heterogeneous UAVs is complex due to their variations. Chen et al. use GLA-MADDPG for quick, safe formation flying instructions, but their approach does not account for specific UAV dynamics and lacks scalability testing [19]. Wu et al. also discuss ACBA for automatic path planning, considering UAV flight capabilities, sensor parameters, area coverage, and obstacle avoidance, though its adaptability to dynamic environments remains unvalidated [20]. Additionally, Wang et al. proposed EIR-MARL, focusing on improving their dynamic collaboration and adaptability while addressing reward sparsity and low exploration efficiency in traditional reinforcement learning [21].

1.1. Problem definition and assumptions

Before presenting and discussing related work, in this section, we formally define the proposed UAV formation path planning problem and provide the context and assumptions of the targeted problem.

Military rotary-wing UAVs are unmanned combat platforms with vertical take-off and landing capabilities, powered by rotary-wing systems. With their flexible deployment, covert surprise defense, and multi-mission adaptability, they are profoundly changing the shape of modern warfare [22]. In military applications, they not only send back real-time battlefield dynamics, but also break through complex terrain to transport materials, or form swarms to carry out saturation attacks. In recent years, the fusion of artificial intelligence and swarm technology has further enhanced their autonomous combat efficiency, making it possible for multi-aircraft coordinated saturation attacks or distributed reconnaissance networks [23]. With the breakthroughs in stealth materials, hydrogen fuel cells, and modularized payload technology, in the future, military rotary-wing UAVs will evolve in the direction of higher intelligence and lower signal characteristics, and the UAV formation control system has become the key to subvert the traditional war mode.

This paper discusses a coordinated saturation attack involving a swarm of UAVs as part of a formation control system. We assume there are multiple launch platforms for the swarm UAVs, each targeting several points that require saturation attacks in a combat area. Each launch platform sequentially deploys numerous UAVs, differing in performance, within a short time frame. These UAVs then form a formation to approach and destroy the same designated target point. The flight process of the swarm UAVs is divided into three phases: the launch phase, the navigation phase, and the attack phase. Our proposed formation control system is primarily applied during the navigation phase of the swarm UAVs.

Launch Phase: This phase focuses on deploying the swarm UAVs within a defined area while maintaining a consistent flight speed.

Navigation Phase: During this phase, the UAVs in formation must quickly and safely traverse through various threat areas to ensure the success of the coordinated saturation attack mission.

Attack Phase: This phase indicates the timeframe when the swarm UAVs are approaching the target point for attack. The UAVs enter a fixed range to signify the commencement of the attack phase.

We have outlined the following scenario: Based on intelligence gathered, we have predicted the terrain and threat areas on the battlefield. Individual UAVs can localize their positions and share this information with friendly UAVs within a specified range. Furthermore, these UAVs can rapidly adjust their flight commands within a limited operational timeframe.

In addition, we have considered several other factors. Our proposed formation control system primarily focuses on the UAV swarm navigation phase, and our experimental process will concentrate on the intermediate stage of formation flight. Swarm UAVs often conduct coordinated saturation attacks, utilizing many low-cost UAVs to target specific points. Consequently, the safety of any individual UAV is not the foremost concern. Instead, our primary objectives are to enhance the system's stability, improve its anti-jamming capabilities, and increase its overall flexibility.

1.2. Related work

In addition to the external airframe limitations related to hardware implementation, the challenges faced during the design of UAV formation mission execution systems can be categorized into three main areas: path planning algorithms, cooperative control for formations, and individual safety assurance for UAVs [13,24]. The remainder of this section will discuss these three categories of formation system design challenges while providing a brief overview of the distributed large-scale joint non-uniform UAV formation real-time path planning system developed in this study.

1.2.1. Path planning algorithm

The UAV path planning problem can be framed as an optimization challenge aimed at identifying a continuous trajectory from the starting point to the endpoint of a mission while adhering to various constraints [25]. This optimal path planning problem for UAVs typically involves path length, optimality, completeness, cost-efficiency, time efficiency, energy efficiency, robustness, safety, and smoothness. It is classified as an NP problem [2].

UAV path planning algorithms can be divided into two main categories: global path planning (GPP) and local path planning (LPP) [26]. The primary distinction between these methods lies in the availability of information about the overall environment and whether the entire mission process is considered. The GPP method is an offline approach that generates paths, typically used in simple, static planning environments. In contrast, the LPP method does not consider global factors. However, it can perform path planning tasks in real time by relying solely on local environmental information, making it suitable for dynamic environments [27,28].

A. Global path planning algorithms

The GPP methods can be categorized into two main types: search-based GPP methods and sampling-based GPP methods. The search-based GPP method involves discretizing a continuous planning environment into a grid map that contains numerous path nodes. Once this grid map is created, the optimal grid paths are identified through a graph search [26]. This approach has been extensively researched and applies to most simple planning environments [29–32]. The sampling-based GPP method generates a continuous path by selecting a specific number of route points within the planning environment. These route points are then connected to form a continuous path. This method is also widely used due to its flexibility regarding both the quantity and positioning of the route points [33–35].

Although the GPP method can guarantee the completeness of the generated optimal paths, its drawbacks are obvious: When the solution environment is complex, the grid density of the search-based GPP method and the number of route nodes of the sampling-based GPP method are difficult to be selected and adjusted [36], and the optimization difficulty of the problem rises sharply when the grid density or the node number is increased. Since the GPP method is an offline path planning method, it is hard to handle dynamic planning environments [37]. Since the GPP method uses the route nodes to represent a path, the smoothness of the path at the path nodes is difficult to guarantee, and since the UAV may not be able to complete the steering maneuver at the path nodes instantaneously, it is difficult to apply this generated path directly to UAVs with an actual physical operating state [24,26]. For joint non-uniform UAV formations, it is difficult to use traditional GPP methods to cope with this dynamic and complex planning environment owing to many individual UAVs and UAV formations operating in the planning space during mission execution.

B. Local path planning algorithms

The LPP method successfully addresses the overall path planning task by generating local paths at each time interval, effectively discretizing the GPP method in the time dimension. This approach transforms the path planning problem into an optimal control problem [38]. Common examples of LPP methods include Rapidly-exploring Random Tree [39–41], Fuzzy Logic Control [28], and Reinforcement Learning [42].

The LPP method generates local paths for each period during partial intervals, offering real-time benefits and adaptability in dynamic environments [43]. However, this method often fails to achieve globally optimal decisions because it relies solely on local environmental information. As a result, local path trajectories may gradually diverge from the globally optimal trajectories during the decision-making process [26]. In more complex environments, the LPP method may cause decision-making agents to become stuck in certain local positions, indirectly leading to failures in the path-planning task. Consequently, the LPP method does not guarantee the generated solutions are complete. Since joint non-uniform UAV formations are designed for executing complex flight tasks efficiently, the risk of mission failure is heightened with the LPP method. Thus, traditional LPP approaches struggle to effectively handle the flight trajectory planning tasks required for these formations. Moreover, the LPP method must generate real-time flight instructions for all UAVs within a specified time frame. As the number of UAVs in the environment increases, the traditional LPP method encounters the ‘curse of dimensionality,’ which severely limits the scalability of joint non-uniform UAV formations [38].

C. Hybrid path planning algorithms

The mission success rate can be improved by hybridizing the GPP method with the LPP method (referred to as HGLPP). This approach ensures that the path planning algorithm can effectively navigate complex dynamic environments while preventing the formation from becoming trapped in a local optimal position [28]. The paths generated by the search-based GPP method often consist of zigzag lines with sharp turns. To enhance the smoothness of these paths, Li et al. integrated the GPP method with a fuzzy inference system and an artificial potential field, making the resulting paths safer and smoother for path-planning algorithms [26]. Yildiz et al. further advanced the robustness and flexibility of UAV formations by combining a consensus-based virtual leader tracking swarm algorithm with a fast exploratory random tree particle swarm optimization route planning algorithm, which considers target distance [44]. Y. Wang improved the efficiency of node searching and the stability of obstacle avoidance in the path planning algorithm by combining the improved A* algorithm with the Fuzzy Dynamic-Window Method algorithm [45]. Additional research has also demonstrated the effectiveness of leveraging the strengths of various path-planning algorithms by combining the GPP and LPP

methods [46–50].

HGLPP typically involves generating global paths first using the GPP method. Once these global paths are established, the path nodes are treated as subgoal points for the LPP method. This approach allows for path planning by continuously addressing local path-planning tasks among these subgoals. While HGLPP effectively enhances the completeness and smoothness of the generated paths, a discrepancy often exists between the actual paths taken and the optimal paths generated. This deviation arises because HGLPP generates the global paths and then issues control commands based on them. However, the kinematic model of the moving entities is not fully accounted for when these global paths are pre-generated, making it challenging for the actual running trajectories to align perfectly with the predetermined global trajectories [28]. Yao et al. highlighted that the deviation between the actual and optimal paths increases with longer paths, more corners, or larger corner angles. This deviation raises the risk of collisions between UAVs and obstacles during their formation [28].

1.2.2. Formation control system

The organization of multiple UAVs in space can be categorized into two control modes: coordinated and cooperative. The coordinated control model features UAVs flying tasks independently from each other. In the coordinated control mode, UAVs completing tasks while avoiding conflicts with other UAVs. The cooperative control mode involves UAVs working together towards a common goal. This mode is typically employed in joint non-uniform formations, where multiple UAVs, each with different functions, collaborate to accomplish complex tasks efficiently in a short amount of time [51]. The multi-UAV formation control system is a crucial component of the cooperative control model. Based on how control commands are generated, this system can be further classified into two types: centralized formation control systems and distributed formation control systems [13].

A. Centralized formation control system

Centralized formation control methods include strategies like the Leader-Follower [52] and virtual structure methods [53,54], which typically designate a leader position for reference within a UAV formation. The other UAVs in the formation adjust their flight states based on their relative positions to the leader, turning the formation challenge into an error control problem [55]. The stability of the formation system characterizes this centralized approach, and it offers advantages such as simplicity and low cost when fewer UAV agents are involved [56]. However, since the UAVs need to maintain the same motion state as the leader, the formation behaves like a rigid structure during operation. Consequently, if there is a deviation in the leader's position, that error is transmitted throughout the entire formation, resulting in weak overall resistance to interference [57]. Additionally, when the formation encounters various obstacles, the control system generally requires adjustments to change the formation's shape to navigate through narrow areas, which significantly limits the flexibility of the mission execution [52]. Moreover, the centralized formation control system has several drawbacks, including a strong dependence on communication conditions, high computational demands on the control center, and unsuitability for managing large clusters of agents. It also has poor scalability and faces challenges in dynamic planning environments [56].

B. Distributed formation control system

Distributed formation control systems function without a central mission control center, establishing an environment where the UAVs operate autonomously without a hierarchical structure. In this innovative framework, the UAVs work together to maintain the overall stability of the formation through robust communication links and sophisticated autonomous algorithms [14]. Among the various approaches to distributed control, two prominent methods stand out: artificial potential field-based methods [58] and behavior-based methods [59–62]. The latter has gained significant traction in real-world applications due to its reduced communication needs and enhanced resilience in dynamic environments. This behavioral approach empowers each UAV to modify its actions based on various quantified behaviors adaptively. These behaviors include avoiding obstacles, exploring designated areas, evading other UAVs, gravitating toward mission targets, preserving their formation positions, and managing individual speeds. By strategically weighing these behaviors, the UAVs can seamlessly coordinate their movements to ensure cohesion within the formation [55]. One of the standout features of distributed formation control systems is their operational simplicity. They are designed for high real-time performance and exceptional scalability, ideally suited for tackling complex, large-scale formation control tasks across non-uniform environments [56]. The system architecture allows for the integration of control command modules directly within the UAV fuselage, resulting in computational capabilities that scale with the size of the formation. This scalability means that the entire system's performance does not rely solely on the capabilities of any single computing unit, allowing for a distributed processing advantage. Furthermore, since distributed formation control systems operate as non-leader control frameworks based on consensus algorithms, they exhibit remarkable flexibility and reliability. They are inherently resilient, with self-healing capabilities that allow them to adapt to changes or failures within the formation quickly. This combination of attributes—flexibility, robustness, reliability, and scalability—positions distributed formation control systems as a powerful solution for modern aerial coordination challenges [55,63].

1.2.3. UAV agent security guarantees

During actual flight, UAVs are frequently influenced by various factors such as changes in air density, air flow, signal delays, signal noise interference, mechanical losses, network bandwidth limitations, multipath effects, the Doppler effect, information propagation errors, human interference, and others. These factors can impact the UAV's maneuverability, ultimately affecting flight safety. Given these challenges, it is crucial to prioritize both stability and robustness in the design of the formation control system for UAVs [18,64]. To enhance flight safety, two primary strategies are commonly implemented: the first involves optimizing the safety of the flight paths generated for the UAVs, ensuring they are as safe and efficient as possible. The second strategy focuses on incorporating a fault-tolerant control system, which enables the UAVs to maintain operational integrity even in the presence of unexpected system failures or disturbances [58].

A. Methods to improve the security of paths

A standard method for enhancing the safety of a UAV's flight path is to add a safety corridor. This safety corridor is defined as a passageway wide enough to encompass the UAV's flight path, ensuring safety while the UAV operates within it. As the UAV navigates the generated path, the back-end system can adjust control commands within this safety corridor to avoid newly detected obstacles or respond to unexpected situations [65]. Ren et al. constructed a tubular safety corridor by connecting consecutive circular regions, enabling the quadrotor UAV to fly safely at an ultra-high speed of 13.7 m/s in a complex forest environment [65]; Hu et al. combined the spherical Said-Ball curve with a novel super eagle optimisation algorithm, and by constructing a tubular safety corridor similar to the Ren et al. tubular safety corridor, further improving the smoothness of the path and the stability of the UAV flight state based on satisfying the high-speed flight of the UAV [66]. Tubular safe corridors have the advantage of being easy to implement in the system design process; however, in nonconvex environments or some complex environments, this method may make the generated paths unable to cover the whole path planning space, resulting in lower quality of the generated paths. For the above reasons, some sets of free convex connected polyhedra are also used to represent safe corridors [67–70].

B. System Fault-Tolerant Control strategies

System Fault-Tolerant Control Strategies (SFTCS) are designed to identify and manage operational errors in individual agents or system components. There are two main approaches to SFTCS: namely passive SFTCS and active SFTCS.

Passive SFTCS relies on the robustness of the system itself, but it usually provides a limited effectiveness, and when operational deviations exceed the maximum range of adjustment available to the system's robustness, the system struggles to ensure overall stability due to errors [63,71].

Active SFTCS contains independent SFTCS [72,73], distributed SFTCS [74–78], and other SFTCS, among which the system frameworks of the two main active SFTCS are shown in Fig. 1 and Fig. 2, where the black dashed box in Fig. 1 denotes the internal operation logic of an individual UAV without SFTCS, and the CGM denotes the control command generation module, the CE denotes the control command execution module, FTC unit denotes the system fault tolerance control module and LNCS denotes the local network command sending module.

The independent SFTCS is distinguished by its ability to avoid using additional local network bandwidth, resulting in less impact on other system users. This makes it more suitable for managing high-density and large-scale UAV formations. In contrast, the distributed SFTCS does place greater demands on local network transmission capacity, but it can reduce the costs of UAV Formation. Equipping only a few UAVs with high-precision sensor modules can significantly improve the stability of the entire formation system.

1.3. Contributions of this study

In general, UAVs are designed to perform point-to-point flight tasks in three-dimensional (3D) space, allowing them to move freely in three directions. However, altering the flight altitude to achieve obstacle and collision avoidance significantly increases energy consumption and introduces issues such as downwash interference [56,79]. For this reason, this paper focuses on controlling UAV formations within a two-dimensional (2D) plane. Solving the problem of UAV swarm formation in 2D space is even more challenging than in 3D space due to the limited options for avoiding obstacles and collisions. If individual UAVs cannot avoid collisions with one another using their Formation Control System (FCS) in 2D space, they still have the option to adjust their altitude to prevent collisions in 3D space. This altitude adjustment leaves some fault-tolerance room for the FCS to a certain extent.

This paper describes a distributed system framework for designing a FCS for UAVs. This framework allows the UAVs to fly safely by using autonomous algorithms and local communication networks along set guidance paths. The UAVs can complete all flight control commands locally, which significantly increases the formation's flexibility and the scalability of the cluster size. The system lets each UAV contact the mission control center during flights. This connection allows them to adjust important details in real-time, such as mission goals, formation layout, and the aircraft's physical parameters. This feature further enhances the FCS's flexibility.

In path planning, we introduce a new method called the global optimal path (guided path) guidance, which combines the GPP method with the LPP method. This combination ensures that the generated paths are complete while also meeting the real-time requirements of the path planning algorithm. Although the guided path resembles the traditional GPP method by being a continuous folded line, this paper enhances it by adding various triggering states for the path nodes. This allows the LPP component of the HGLPP

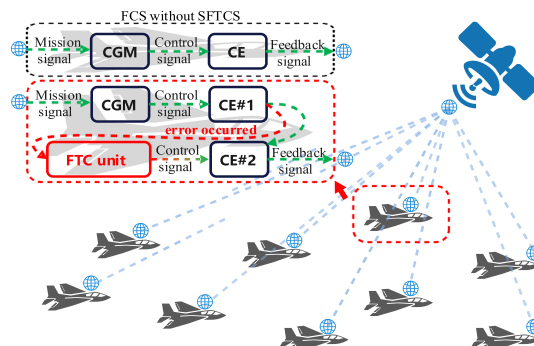


Fig. 1. Schematic of independent SFTCS.

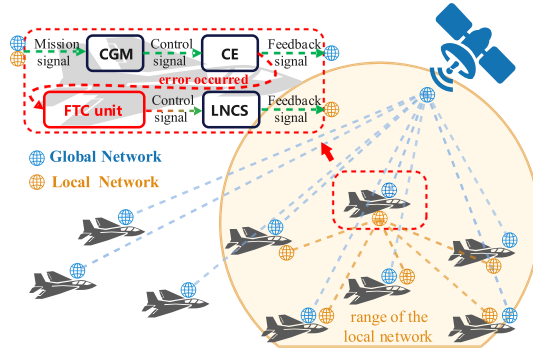


Fig. 2. Schematic of distributed SFTCS.

method to dynamically select optimal sub-target nodes, thus improving the flexibility of the formation system. This approach helps to decrease the local meandering phenomenon appeared in UAV formations, especially in areas with dense aircraft swarms. Additionally, this paper details the planning of an agent's local path through adjustments in the agent's flight instructions. This process takes into account the physical kinematic state of the aircraft and retains essential physical properties, such as inertia, during modeling. By generating flight instructions repeatedly over a period, we significantly enhance the smoothness and safety of the flight paths, leading to experimental results that hold practical significance.

The distributed large-scale joint non-uniform UAV formation real-time path planning system proposed in this paper pays excellent attention to the security of UAV agents within the formation. The guidance path proposed herein is not a collision-free path in traditional sense, but a guidance channel with a larger width but fewer obstacles, and the individuals within the formation avoid other UAVs and those small obstacles during the flight by using the LPP method. This approach can reserve more room for the UAV agents to freely adjust their flight status, and improves the safety of the agents' individuals within the formation. Since we use a distributed system framework, the system itself has a certain degree of error tolerance, i.e., the system itself possesses passive SFTCS. We prevent possible planning errors in the LPP part of the FCS in advance, and improve the stability of the UAV by introducing local interaction partially degraded; we also add a simple active SFTCS in the FCS to increase the safety of the agents within the formation by generating flight control instructions twice. Some other system design details will be explained in detail in the FCS introduction section.

The main contributions of this paper are as follows:

- (1) We propose a path planning algorithm for large-scale heterogeneous UAV formations. This algorithm can handle the problem of multiple formations executing multiple tasks. This algorithm has a significant advantage over other algorithms because it allows different UAVs in the same formation to differ.
- (2) This algorithm divides the path planning task into global path guidance, local path generation, and local path correction. This paper focuses on the latter two parts because general GPP methods can steer the global path. This design retains most of the advantages of the GPP and LPP methods.

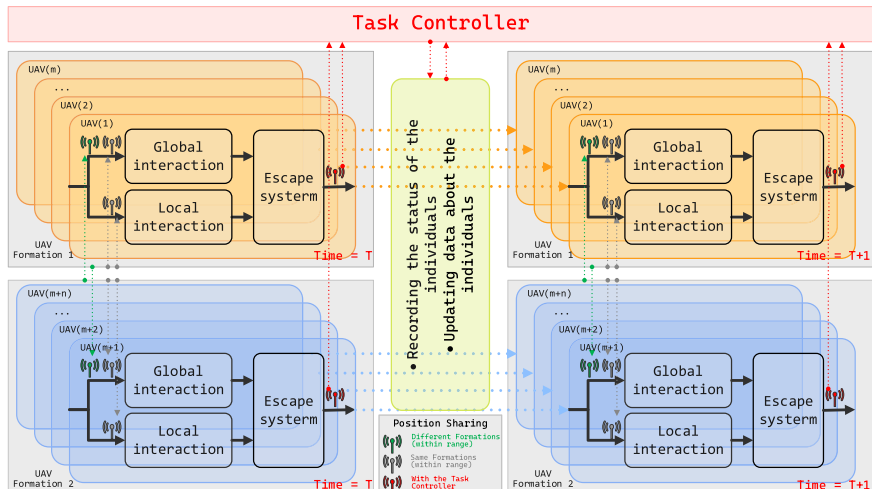


Fig. 3. System framework of the FCS.

- (3) The aim of the algorithm design and the need for the problem addressed are strong scalability and robustness. Therefore, we have designed a behavior-based approach to formation control. The innovation of the method is the low information requirements (including accuracy requirements) for neighboring UAVs. In addition, the feature that no real-time information is required provides parallel computing for large-scale formation command generation.
- (4) The path planning system contains two types of SFTCS since behavior-based formation control methods do not provide complete security. The system itself possesses passive SFTCS, which is why it is highlighted. Secondly, we add active SFTCS after generating local paths to improve safety further.

The rest of the paper is organized as follows: Chapter 2 details the operation logic of the distributed large-scale joint non-uniform UAV formation real-time path planning system at both the system and path planning algorithm aspects; Chapter 3 is the experimental chapter, in which the effectiveness of the system in terms of obstacle avoidance, guidance, convergence, freedom of scale, formation change, scale pressure, robustness is verified through a large number of rational and repetitive experiments, and the ablative experiments to verify the design and rationality of the FCS; Chapter 4 is the concluding chapter.

2. The real-time path planning method for UAV formations

2.1. Formation control system

The FCS consists of two key components: the locally deployed Formation Control Module (FCM) and the Task Controller (TC), as illustrated in Fig. 3. In two groups of aircraft, the yellow box and blue box represent the FCM for each UAV within those groups. The FCM is embedded within each UAV as an internal system, tasked with generating, adjusting, and executing flight control commands based on the pre-defined flight trajectory and employing an autonomous algorithm. The red box represents the TC, which is responsible for updating the UAV's data—such as mission details, formation information, and UAV parameters—during mission execution. Indeed, if there is no need to modify the UAV's data during the mission, the TC part can be removed from the FCS, thus enabling the individual UAVs to execute the formation mission fully offline.

The FCM consists of three key components: the global interaction part, the local interaction part, and the escape system. In Fig. 3, the dotted lines illustrate the information-sharing system. The green dotted line represents information sharing between UAVs from different formations within a specific range, while the grey dotted line denotes information sharing among UAVs within the same formation, which relies solely on the local area network and has stringent timing requirements for shared information. The red dotted line indicates the information exchange between the UAVs and the task control center, which can occur over unlimited distances. As depicted in Fig. 3, the local interaction component of the FCM only requires access to the state information of other UAVs within the same formation. In contrast, the global interaction component necessitates additional information exchange with individual UAVs from other formations. The escape system operates independently of the interaction components; it activates when an individual UAV is at a high risk of collision, providing an extra layer of flight safety for the UAVs.

2.2. Mathematical modelling of UAVs

In this paper, a UAV is abstracted as a smooth sphere, and the radius of the i th UAV is denoted as R_i . Two UAVs are regarded as colliding when the radius of the i th UAV and the j th UAV is less than $R_i + R_j$. Multiple UAV formations usually exist in the planning space, and multiple different UAVs can be assigned to the same formation, since this work has different treatments for UAVs in the same formation versus different formations, the position of the i th UAV in the c th formation at the moment t th is noted to be $\mathbf{P}_{c,i}(t)$, then

$$\mathbf{P}_{c,i}(t) = \left(P_{x,c,i}(t), P_{y,c,i}(t) \right), \quad i = 1, 2, \dots, N_c, \quad c = 1, 2, \dots, N, \quad (1)$$

where $P_{x,c,i}(t)$, $P_{y,c,i}(t)$ denote the two components of $\mathbf{P}_{c,i}(t)$ in the horizontal direction, respectively; N_c denotes the number of UAVs in the c th UAV formation; and N denotes the number of formations in the planning space.

To better reflect the flight state of the UAV in reality, this paper simulates the existence of inertia in the UAV, the effect of inertia in the moving trajectory at the same time by the UAV's flight speed and acceleration, the effect of inertia in the trajectory of the UAV, the velocity and acceleration of the i th UAV in the c th formation at moment t th are noted to be $\mathbf{V}_{c,i}(t)$ and $\mathbf{A}_{c,i}(t)$, respectively. There is an upper limit to the flight speed and acceleration of each UAV, the upper limit to the velocity and acceleration of the i th UAV in the c th formation at moment t th are noted to be $\tilde{\mathbf{V}}_{c,i}$ and $\tilde{\mathbf{A}}_{c,i}$, respectively, particularly, both $\tilde{\mathbf{V}}_{c,i}$ and $\tilde{\mathbf{A}}_{c,i}$ of each UAV may differ.

$\mathbf{V}_{c,i}(t)$ calculated according to Eq. (2):

$$\mathbf{V}_{c,i}(t) = \begin{cases} \min\left\{ \mathbf{V}_{c,i}(t-1) + \mathbf{A}_{c,i}(t), \tilde{\mathbf{V}}_{c,i} \times \frac{\mathbf{V}_{c,i}(t-1) + \mathbf{A}_{c,i}(t)}{|\mathbf{V}_{c,i}(t-1) + \mathbf{A}_{c,i}(t)|} \right\} & t \geq 1 \\ [0, 0] & t = 0 \end{cases}. \quad (2)$$

Based on the velocity of the UAV at the current moment in time, the position of the i th UAV in the c th formation at moment t th calculated according to Eq. (3):

$$\mathbf{P}_{c,i}(t) = \mathbf{P}_{c,i}(t-1) + \mathbf{V}_{c,i}(t), \quad i = 1, 2, \dots, N_c, \quad c = 1, 2, \dots, N, \quad t \geq 1, \quad (3)$$

where N_c denotes the number of UAVs in the c th UAV formation; and N denotes the number of formations in the planning space.

According to Eq. (3), without considering the uncertainty, only the $\mathbf{A}_{c,i}(t)$ of the UAVs at each moment needs to be provided, and the position of the UAVs at each moment can be calculated based on the initial position of the UAVs, so the task of flying the whole UAV swarm in formation can be accomplished by providing a reasonable $\mathbf{A}_{c,i}(t)$ of each UAV. This paper generates the $\mathbf{A}_{c,i}(t)$ of individual UAVs at each moment in time based on FCS by exchanging the relevant state information of the UAVs in the local range of the cluster to complete the task of formation flying of the whole UAV cluster.

2.3. Formation control module

The formation control module consists of three key components: the global interaction part, the local interaction part, and the escape system.

The global interaction component is influenced by both the UAV's own formation and the formations of other UAVs within a specific range. This interaction is crucial for the formation controller, as it defines the feasible space for the mission over time and guides the UAV formation to complete the mission progressively, step by step. The local interaction part of single UAVs is only acted by UAVs within a specific range of the current formation. Its primary purpose is to help the UAV formation achieve stable and efficient flight by adjusting the UAV's flight state. The feature of the local interaction part is that it has a low influence on the UAV's flight attitude and is not affected by UAVs outside the formation. The escape systems provide further security for FCM.

The FCS can be divided into three components: global optimal guidance, local path generation, and local path correction. This section focuses specifically on local path generation and local path correction. Readers must notice the known variables used in each equation as they explore the FCM. First, local path generation relies solely on the state information of other UAVs from the previous moment. This parallel processing is a key feature of the FCM, enabling autonomous control of large-scale UAV formations. Second, local path generation only takes into account the positions and velocities of other UAVs within a specified range, which contributes to the FCM's low communication requirements. Additionally, the escape system's flight commands are executed at a consistent altitude, allowing for the possibility of avoiding collisions among UAVs by making altitude adjustments.

2.3.1. Global interaction part

The global interaction part consists of the separated interaction part (SI) and the guided interaction part (GI):

2.3.1.1. Separated interaction part. The effect of SI is that when other UAVs are within a specific range of a particular UAV, that UAV will tend to move away from the positions of the other UAVs. This behavior helps to avoid collisions and contributes to the overall allocation of available space for the formation mission over time. The SI of the $i + 1$ th UAV in the c th formation at the t th moment is denoted as:

$$\mathbf{Fs}_{c,i}(t+1) = \frac{\sum_{m=1}^N \sum_{n=1}^{N_m} \left(\delta_{c,i,m,n}(t) \times \frac{\mathbf{P}_{c,i}(t) - \mathbf{P}_{m,n}(t)}{|\mathbf{P}_{c,i}(t) - \mathbf{P}_{m,n}(t)|^2} \right)}{\sum_{m=1}^N \sum_{n=1}^{N_m} \delta_{c,i,m,n}(t)}, \quad i = 1, 2, \dots, N_c, c = 1, 2, \dots, N, \quad (4)$$

where N_c denotes the number of UAVs in the c th UAV formation; N denotes the number of formations in the planning space; $\delta_{c,i,m,n}(t)$ is a logical parameter that takes the value of 0 or 1; The formula for $\mathbf{Fs}_{c,i}(t)$ in Eq. (4) can be interpreted simply as a weighted average of the effect of moving away from other UAVs within a certain range, and the closer the distance the greater the weights.

$\delta_{c,i,m,n}(t)$ is used to detect whether the n th UAV in the m th formation is located within a high collision risk area of the i th UAV in the c th formation at the t th moment, and it is expressed as:

$$\delta_{c,i,m,n}(t) = \begin{cases} 1 & 0 < |\mathbf{P}_{c,i}(t) - \mathbf{P}_{m,n}(t)| \leq R_s, \\ 0 & \text{else} \end{cases}, \quad (5)$$

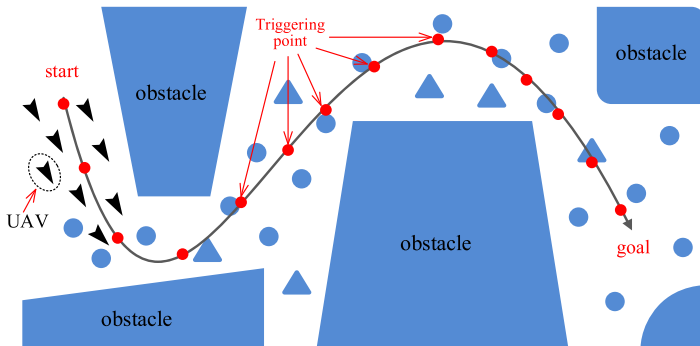


Fig. 4. Schematic diagram of a guided path in a planned space.

where R_s indicates the radius at a UAV that generates the SI effect. For different performance UAVs, there are theoretical differences in the value of R_s , but for convenience of calculation in this paper, all UAVs have the same radius for generating the SI effect, which is uniformly denoted as R_s .

2.3.1.2. Guide interaction part. Traditional UAV formation control algorithms direct the formation toward the target point by attracting individual UAVs to their target positions [14]. This approach is appropriate for scenarios with few obstacles in the planning space, especially when those obstacles are small. However, when faced with significant and irregular obstacles, individual UAVs in the formation risk getting stuck in localized positions. This paper presents a guidance path away from large-size obstacles and uses the guidance path to guide the UAV formation efficiently toward the mission target point.

As illustrated in Fig. 4, several larger obstacles and numerous smaller ones are situated between the task start point and the task endpoint. Notably, there are only minor obstacles along the grey path, which is referred to as the guide path of the cluster in this paper. The guided paths can be generated simply and efficiently using the GPP method; therefore, they are not the primary focus of this research, and all guided paths in the experiments have been predetermined. When there are no significant obstacles in the planning space, the guided path can be established as a straight line connecting the task start point to the task goal point. Consequently, the guided path-based formation task execution method proposed in this paper offers greater flexibility and adaptability to environmental conditions compared to traditional methods.

The guide path consists of several path nodes, which are called trigger points here, and the trigger points are uniformly distributed on the guide path so that the guide path can be expressed as:

$$\mathbf{Lp}_c = \{\mathbf{Tp}_{c,1}, \mathbf{Tp}_{c,2}, \dots, \mathbf{Tp}_{c,Nt_c}\}, c = 1, 2, \dots, N, \quad (6)$$

where Nt_c denotes the number of trigger points that compose the guide path of the c th UAV formation; N denotes the number of formations in the planning space, this paper defaults to direct UAVs with the same path to be in the same formation.

Trigger points on the guide path exist in two states, namely invalid trigger points and untriggered trigger points, and the trigger state for each UAV is recorded separately for trigger points on the guide path. A trigger radius exists for the trigger point, denoted as Rtp . For single UAVs, when the UAV enters within the trigger radius of a trigger point, this trigger point and its previous trigger points are invalidated. Each UAV has a unique trigger point among all the untriggered trigger points that generate GI with the current UAV. We write down the trigger for generating GI for the i th UAV in the c th formation at moment t as $Ptp_{c,i}(t)$, the set in which this point is located is denoted:

$$Ptp_{c,i}(t) \in \{\mathbf{Tp}_{c,h} \mid |\mathbf{P}_{c,i}(m) - \mathbf{Tp}_{c,h}| > Rtp\}, m = 1, 2, \dots, t, n = h + 1, h + 2, \dots, Nt_c, \quad (7)$$

where Nt_c denotes the number of trigger points that compose the guide path of the c th UAV formation. Generally, $Ptp_{c,i}(t)$ selects the trigger point in this set that is closest to $\mathbf{P}_{c,i}(t)$.

The GI of the UAV is expressed as:

$$\mathbf{Fg}_{c,i}(t+1) = Ptp_{c,i}(t) - \mathbf{P}_{c,i}(t). \quad (8)$$

2.3.2. Local interaction part

This local interaction comprises two components: the alignment interaction (AI) and the cohesion interaction (CI).

2.3.2.1. Alignment interaction part. When UAVs in an area maintain similar speeds, their speed differences are minimal, resulting in a stable UAV formation that reduces the likelihood of confusion within the group. The AI of the $i + 1$ th UAV in the c th formation at the t th moment is denoted as:

$$\mathbf{Fa}_{c,i}(t+1) = \frac{\sum_{n=1}^{N_c} (\varphi_{c,i,n}(t) \times \mathbf{V}_{c,n}(t))}{\sum_{n=1}^{N_c} \varphi_{c,i,n}(t)} - \mathbf{V}_{c,i}(t), \quad (9)$$

where N_c denotes the number of UAVs in the c th UAV formation; $\varphi_{c,i,n}(t)$ is a logical parameter that takes the value of 0 or 1; The calculation in Eq. (9) can be interpreted simply as a tendency for the UAV's speed to be consistent with the average speed of other UAVs within a certain range.

$\varphi_{c,i,n}(t)$ is used to detect whether the n th UAV in the c th formation is located within the surrounding area of the i th UAV in the c th formation at the t th moment. In this surrounding area, other UAVs are currently close to this UAV, posing no immediate threat to its safety. However, they have the potential to move into an area that could present a high risk of collision over time. $\varphi_{i,n}^{c,t}$ is expressed as:

$$\varphi_{c,i,n}(t) = \begin{cases} 1 & R_s < |\mathbf{P}_{c,i}(t) - \mathbf{P}_{c,n}(t)| \leq Ra, \\ 0 & \text{else} \end{cases}, \quad (10)$$

where R_s indicates the radius at a UAV that generates the SI effect; Ra indicates the radius at a UAV that generates the AI effect. For different performance UAVs, there are theoretical differences in the value of Ra , but for convenience of calculation in this paper, all UAVs have the same radius for generating the AI effect, which is uniformly denoted as Ra .

2.3.2.2. Cohesion interaction part. Maintaining a relatively compact cluster structure can help to help UAV formations efficiently pass through some of the complex formation planning environments, while keeping the UAV body safe. The CI of the $i + 1$ th UAV in the c th formation at the t th moment is denoted as:

$$\mathbf{Fc}_{c,i}(t+1) = \frac{\sum_{n=1}^{N_c} (\gamma_{c,i,n}(t) \times (\mathbf{P}_{c,n}(t) - \mathbf{P}_{c,i}(t)))}{\sum_{n=1}^{N_c} \gamma_{c,i,n}(t)} - \mathbf{V}_{c,i}(t), \quad (11)$$

where N_c denotes the number of UAVs in the c th UAV formation; $\gamma_{c,i,n}(t)$ is a logical parameter that takes the value of 0 or 1.

$\gamma_{c,i,n}(t)$ is used to detect whether the n th UAV in the c th formation is located within the surrounding area of the i th UAV in the c th formation at the t th moment. When multiple other UAVs in the formation are present in the area but are far from the current UAV, it suggests that the current UAV may have shifted away from the center of the formation or has separated from it. In such cases, the UAV must rejoin the formation by adjusting its flight position. $\gamma_{c,i,n}(t)$ is expressed as:

$$\gamma_{c,i,n}(t) = \begin{cases} 1 & 0 < |\mathbf{P}_{c,i}(t) - \mathbf{P}_{c,n}(t)| \leq R_c \\ 0 & \text{else} \end{cases}, \quad (12)$$

where R_c indicates the radius at a UAV that generates the CI effect. For different performance UAVs, there are theoretical differences in the value of R_c , but for convenience of calculation in this paper, all UAVs have the same radius for generating the CI effect, which is uniformly denoted as R_c .

2.3.3. Effect analysis of different interactions

The action of SI is illustrated in Fig. 5(a). In this figure, the red UAV and the blue UAV are affected by SI because there is only one other UAV—the green UAV—within a range of R_s . The green UAV is positioned to the right front of the red UAV, causing the red UAV to decelerate and maneuver towards the left rear. Conversely, since the green UAV is located at the right rear of the blue UAV, the blue UAV will accelerate towards the left front in response. As for the green UAV, it detects two UAVs within its range, leading to a combined force dictated by the SI. By comparing the triangular formation of the three UAVs before and after experiencing SI in Fig. 5(a), we observe that the UAVs' formation can significantly decrease cluster density, thereby minimizing the likelihood of collisions between UAVs.

Fig. 5(b) shows the change in flight posture of a UAV cluster subjected to GI, with different colored UAVs being affected by different colored trigger points. Where GI enables UAV clusters to fly close to each other and towards the mission target point during the planning process of a formation mission.

The SI makes the UAVs maintain a relatively sparse and safe cluster structure, while the GI will make the UAVs in the cluster close to each other while guiding the cluster toward the mission's target point. When the two interactions in the global interaction are balanced, the UAV cluster can move towards the target point with a safe relative positional structure to complete the formation control task of the UAV formation. Thus, the global interaction plays the central control role in the UAV formation task.

Fig. 6(a) illustrates the change in flight attitude of the UAV after being subjected to AI. In Fig. 6(a), no other UAVs within the radius of R_s of the green UAV exist, indicating that the UAV itself is in a relatively safe position. Since there is a difference between the green UAV's speed and the average speed of the UAVs within the range of R_s to R_a , with the operation of the UAV formation, there exists the possibility that this UAV will enter the high collision risk area of other UAVs, so AI is implemented on it. In Fig. 6(a), the original speed in grey is adjusted to the actual speed in red, which reduces the possibility of confusion in the speed of the UAVs in the formation due to the green UAV intruding into the high collision risk area of the other UAVs and thus causing confusion in the speed of the UAVs in the formation. Since AI is a local interaction, its effect on the UAV's flight attitude is small, and this alignment process is performed slowly during the formation planning process.

Fig. 6(b) shows the flight attitude change of the UAVs after being subjected to CI. The UAVs at the back of the formation accelerate towards the center of the formation, while the UAVs at the front of the formation decelerate and merge with the other UAVs into the UAV formation. Since CI is a local interaction, its impact on the UAV's flight attitude is small, and this coalescence process is also

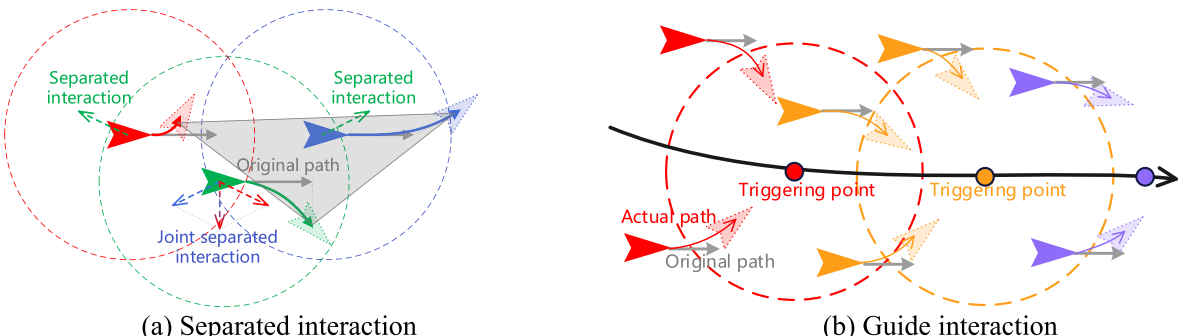


Fig. 5. Schematic of the global interaction.

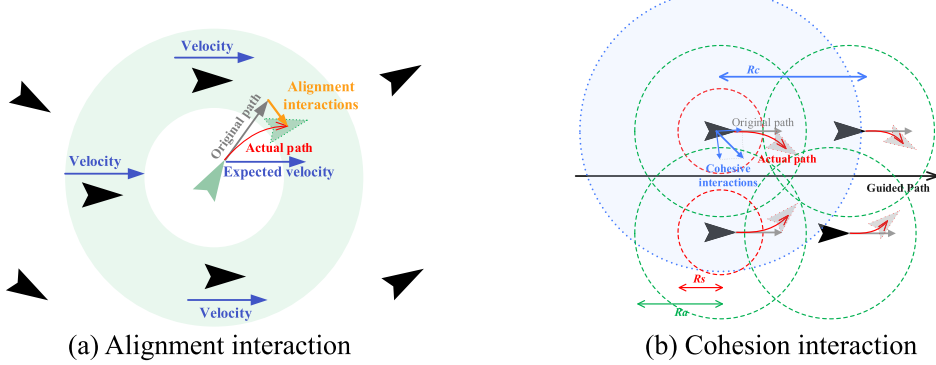


Fig. 6. Schematic of the local interaction.

carried out slowly during the formation planning process.

2.3.4. wt setting and combination of interactions

The weight design of interactions must consider both the range of values and their distribution, as these factors play a crucial role in the formation planning process. Therefore, a reasonable weight combination strategy is essential for successful formation planning. The combination method of interaction roles can be expressed as:

$$\mathbf{A}_{c,i}(t+1) = \frac{\omega s \cdot a_{c,i}(t) \cdot \frac{F_{s_{c,i}}(t)}{|F_{s_{c,i}}(t)|} + \omega g \frac{F_{g_{c,i}}(t)}{|F_{g_{c,i}}(t)|} + \omega a \frac{F_{a_{c,i}}(t)}{|F_{a_{c,i}}(t)|} + \omega c \frac{F_{c_{c,i}}(t)}{|F_{c_{c,i}}(t)|} \tilde{\mathbf{A}}_{c,i}}{\omega s + \omega g + \omega a + \omega c}, \quad (13)$$

where ωs , ωg , ωa , ωc is the combination weights of SI, GI, AI and CI; $\tilde{\mathbf{A}}_{c,i}$ is the upper limit of acceleration for the i th UAV in the c th formation, $a_{c,i}(t)$ denotes a weight value.

During the global interaction process, SI provides obstacle avoidance capability for the UAV swarm, and GI drives the formation to complete the planning task, so ωs and ωg should be given a larger combination weight. Due to the superposition of $F_{s_{c,i}}(t)$ and $F_{g_{c,i}}(t)$ exist in the area of action, the value of ωs should be higher than ωg based on the full consideration of UAV flight safety. AI and CI play a role in adjusting the UAV attitude during formation control, and this action process should be carried out without affecting the global interactions, so ωa and ωc need to be given a smaller combined weight, which should be much lower than ωs and ωg . Since ωs , ωg should be endowed with larger combination weights, to prevent the UAV interactions from large changes in the interaction's role boundary, in this paper, linearisation of $F_{s_{c,i}}(t)$ is done to ensure that the value of ωs is higher than that of ωg based on the reduction of the magnitude of change of $F_{s_{c,i}}(t)$ in the boundary, which is referred to herein as linear separating force.

The $a_{c,i}(t)$ can be expressed as:

$$a_{c,i}(t) = 1 - \min \left\{ \frac{|\mathbf{P}_{c,i}(t) - \mathbf{P}_{m,n}(t)|}{R_s} \mid n=1, 2, \dots, i-1, i+1, \dots, N_m, m=1, 2, \dots, N \right\}, \quad (14)$$

where R_s indicates the radius at a UAV that generates the SI effect; N_m denotes the number of UAVs in the m th UAV formation; N denotes the number of formations in the planning space.

2.3.5. Escape system

Behavior-based UAV swarm formation methods do not fully ensure the flight safety of individual UAVs. Therefore, this paper introduces an escape system to the FCM. This system assists individual UAVs within the formation in avoiding collisions by modifying flight instructions when they are at a high risk of collision. The flight instructions generated secondarily by the escape system can be expressed as:

$$\mathbf{A}_{c,i}(t+1) = \{\tilde{\mathbf{A}}_{c,i} \cdot (\cos\theta, \sin\theta) \mid D(\mathbf{P}_{c,i}(t+1), \theta, 1) \geq D(\mathbf{P}_{c,i}(t+1), \phi, 1), \theta \in (0, 2\pi), \phi \in (0, 2\pi)\}, \quad (15)$$

where $\tilde{\mathbf{A}}_{c,i}$ is the upper limit of acceleration for the i th UAV in the c th formation; $D(\mathbf{P}_{c,i}(t), \theta, k)$ denotes a constant related to the initial position of the UAV and a constant parameter k .

Eq. (15) only regenerates $\mathbf{P}_{c,i}(t+1)$ at $D(\mathbf{P}_{c,i}(t+1), \theta, 0) < Re$ to help individual UAVs in the formation avoid collisions with other UAVs, where Re indicates the escape radius of a UAV.

$D(\mathbf{P}_{c,i}(t), \theta, k)$ can be expressed as:

$$D(\mathbf{P}_{c,i}(t), \theta, k) = \min \{ |\hat{\mathbf{P}}_{c,i}(t, \theta) - \mathbf{P}_{m,n}(t)| \mid n=1, 2, \dots, i-1, i+1, \dots, N_m, m=1, 2, \dots, N \}, \quad (16)$$

where N denotes the number of formations in the planning space; N_m denotes the number of UAVs in the m th UAV formation; $\hat{\mathbf{P}}_{c,i}(t, \theta)$

represents a position at time t calculated based on a given angle value θ .

$\hat{\mathbf{P}}_{c,i}(t, \theta)$ can be expressed as:

$$\hat{\mathbf{P}}_{c,i}(t, \theta) = \mathbf{P}_{c,i}(t) + \tilde{\mathbf{A}}_{c,i} \cdot (\cos\theta, \sin\theta), \quad (17)$$

where $\tilde{\mathbf{A}}_{c,i}$ is the upper limit of acceleration for the i th UAV in the c th formation.

3. FCS-related experiments

To fully validate the effectiveness of the algorithm proposed herein, the FCS is fully simulated and validated in terms of obstacle avoidance capability, guidance path guidance capability, formation convergence speed, formation size change capability, separation and recombination capability between formations, formation size stress test under fixed scenarios, and robustness. Besides, reasonable ablation experiments are carried out in the experimental part to verify the reasonableness of FCS design by sequentially separating the constituent modules of FCS. The simulation environment used here is 'Windows 10 (64-bit) 23H2', 'i5-13600KF CPU 32GB', and the simulation platform is 'Matlab2023b', detailed information about the experimental scenarios for all experiments, detailed data for each set of experiments and a demonstration video with timer are given in the Supplementary Material.

To fully simulate the differences between the UAVs within the UAV formation in the natural environment, the UAVs' parameters in the simulation experiments are independent. The initial position of the UAV and specific parameters are chosen to be random values within a certain range, and random factors' influence on the formation control algorithm is reduced through multiple repetitive experiments in this paper; the relevant parameters of the UAVs and the FCS are shown in [Table 1](#).

From distance, time, speed, and security perspectives, this paper statistically calculates the following performance indicators to evaluate the FCS's ability to control formation in different scenarios. The statistical indicators used herein are shown in [Table 2](#). [Table 3](#) describes some symbols used in the formulas for the indicators in [Table 2](#).

Unless otherwise stated, when calculating the AMD, ART, AVCR, AVIR, AWR, ACR, and AESR, the UAVs in the scenarios are considered to be in the same formation. This is because their role of those values in all simulation experiments is the same in different formations.

3.1. Environmental adaptability

3.1.1. Experiment 1: adaptation to different global optimal guided paths

Since the FCS needs to preset a guidance path to guide the formation in flight, this experiment investigates the effect of different guidance paths on the FCS. Three kinds of guidance paths have obvious characteristics: non-distinctive straight lines, trapezoidal folding lines, and smooth sinusoidal curves. The specific guidance path settings are shown in [Fig. 7](#). Since the FCS only provides flight instructions for the navigation phase of the formation. During the initialization phase, we randomly assign formation individuals around the starting point, provide them with a random initial velocity, and then intercept the stable flight process after a while (20 s) for data analysis.

[Fig. 8](#) illustrates the trajectory mapping diagrams for the UAV swarm operation under three different guidance paths. The time nodes corresponding to each color are indicated in the figure. The black dotted lines represent the guidance paths, while the fluorescent green sections highlight the waypoints of the UAVs within the formation, which are positioned at distances ranging from $0.8Rtp$ to Rtp units from the guidance paths. There are no waypoints located more than Rtp units away from the guidance paths.

According to [Fig. 8](#), the width of the formation trajectory will gradually narrow during the formation operation. This reduction in width indicates that the volatility of the formation trajectory is decreasing, which suggests that the structural tightness and stability of the formation are improving under the control of the FCS, and this improvement reflects the effectiveness of the FCS. Additionally, the width of the trajectory shows significant changes when the formation size is smaller, while it remains almost unchanged for larger

Table 1
The parameter setting of UAVs and FCS.

Parameters	Symbol in this paper	Range or Value
Maximum Acceleration	$\tilde{\mathbf{A}}_{c,i}$	$7 \sim 10m/s$
Maximum Velocity	$\tilde{\mathbf{V}}_{c,i}$	$7 \sim 10m/s^2$
Escape Radius	Re	$3m$
Separate Interaction Radius	Rs	$50m$
Alignment Interaction Radius	Ra	$75m$
Cohnsive Interaction Radius	Rc	$90m$
Separate Interaction Weights	ω_s	1.2
Guide Interaction Weights	ω_g	1.0
Alignment Interaction Weights	ω_a	0.1
Cohnsive Interaction Weights	ω_c	0.1
Trigger Radius	Rtp	$50m$
UAV Radius	$R_{c,i}$	$1mm$
Velocity update frequency	\sim	$10hz$

Table 2

Statistical indicators utilised.

Indicator name	Abbreviations	Indicator description	Indicator formula or symbol
minimum distance	MD	MD is defined as the distance between the closest UAV and the current UAV, which should be as small as possible to make the UAV swarm structurally tight while ensuring the safety of the UAV flight.	$\begin{aligned} Mr_{c,i}(t) &= \min\{ P_{c,i}(t) - \\ &P_{m,n}(t) \mid n = 1, 2, \dots, i-1, i+1, \dots, N_m \\ &m = 1, 2, \dots, N\} \end{aligned}$
Average minimum distance	AMD	The AMD is relative to the formation as a whole. The smaller the AMD, the more compact the formation as a whole is and the denser the UAV formation. If not considering the time dimension, the AMD can reflect the compactness of the formation's structure during the whole process.	$\begin{aligned} AMr_c(t) &= \frac{1}{N_c} \cdot \sum_{i=1}^{N_c} Mr_{c,i}(t) \\ AMr_c &= \frac{1}{T_c \cdot N_c} \cdot \sum_{i=1}^{N_c} \sum_{t=1}^{T_c} Mr_{c,i}(t) \end{aligned}$
Average running time	ART	ART reflects the extent to which the UAV formation's overall speed slows down due to interference from other formations. Given the same total mission length, a longer ART indicates a greater degree of influence from other formations and a lower efficiency of mission execution.	$AT_c = \frac{T_c}{L_c}$
Velocity change rate	VCR	VCR is defined as the ratio of the UAV velocity change to the maximum acceleration at moment t . This value is smaller when the UAV is flying in a stable state. In addition, when the formation's operational state is at a standstill, this value may also be smaller.	$Vc_{c,i}(t) = \frac{ \dot{V}_{c,i}(t) - \dot{V}_{c,i}(t-1) }{\tilde{A}_{c,i}}$
Average velocity change rate	AVCR	The lower the average VCR, the more stable the formation structure is, meaning no large-scale chaos occurred in the UAV formation. If the time dimension is not considered, then the AVCR can reflect the degree of stability of the formation structure during the whole operation. This value can also serve to observe if the formation operation has reached a standstill.	$\begin{aligned} AVc_c(t) &= \frac{1}{N_c} \cdot \sum_{i=1}^{N_c} Vc_{c,i}(t) \\ AVc_c &= \frac{1}{T_c \cdot N_c} \cdot \sum_{i=1}^{N_c} \sum_{t=1}^{T_c} Vc_{c,i}(t) \end{aligned}$
Velocity impact rate	VIR	VIR is the UAV's speed ratio to the maximum speed at moment t . A smaller value reflects that the UAV is flying faster, indirectly reflecting the high efficiency of mission execution. This value ranges from [0,1].	$Vi_{c,i}(t) = \frac{ \dot{V}_{c,i}(t) }{\tilde{V}_{c,i}}$
Average velocity impact rate	AVIR	A smaller AVIR represents a faster flight speed of the formation, which indirectly indicates a high efficiency of mission execution. If the time dimension is not considered, the AVIR can reflect the formation's efficiency in executing its tasks over the entire operation.	$\begin{aligned} AVi_c(t) &= \frac{1}{N_c} \cdot \sum_{i=1}^{N_c} Vi_{c,i}(t) \\ AVi_c &= \frac{1}{T_c \cdot N_c} \cdot \sum_{i=1}^{N_c} \sum_{t=1}^{T_c} Vi_{c,i}(t) \end{aligned}$
Average Warning Rate	AWR	AWR is defined as the proportion of other UAVs in the UAV formation that enter the escape radius of a UAV over the entire flight, where a smaller value makes the formation safer for individual UAVs.	$\begin{aligned} AWr_c &= \frac{1}{T_c \cdot N_c} \cdot \sum_{i=1}^{N_c} \sum_{t=1}^{T_c} Wr_{c,i}(t) \\ \text{where } Wr_{c,i}(t) &= \begin{cases} 1 & Mr_{c,i}(t) \leq Re \\ 0 & \text{else} \end{cases} \end{aligned}$
Average Collision Rate	ACR	ACR is defined as the percentage of UAV collisions occurring throughout the flight of a UAV formation, where a smaller value makes the formation safer for individual UAVs.	$\begin{aligned} ACr_c &= \frac{1}{T_c \cdot N_c} \cdot \sum_{i=1}^{N_c} \sum_{t=1}^{T_c} Cr_{c,i}(t) \\ \text{where } Cr_{c,i}(t) &= \begin{cases} 1 & Mr_{c,i}(t) \leq R_{c,i} \\ 0 & \text{else} \end{cases} \end{aligned}$
Average Escape Success Rate	AESR	AESR is the ratio of ACR to AWR; given the same AWR, a larger AESR indicates that the FCM's ability to deal with hazardous situations is more remarkable.	$AESr_c = \frac{1 - ACr_c}{AWr_c}$

Table 3

Explanation of some symbols of the indicator formulae in Table 2.

Symbol	Description of symbols
R_s	Radius of the UAV generating SI
Re	Escape radius of the UAV
N	The number of formations in the planning space
N_c	The number of UAVs in the c th UAV formation
T_c	Runtime for the c th UAV formation to complete its mission in its entirety
L_c	Total mission length of the c th UAV formation
$\tilde{A}_{c,i}$	Acceleration limit for the i th UAV in the c th formation
$\tilde{V}_{c,i}$	Velocity limit for the i th UAV in the c th formation
$R_{c,i}$	Radius of the i th UAV in the c th formation

formation sizes. This phenomenon reflects that the FCS can adaptively adjust the density of the formation. According to Fig. 8, most waypoints that are farther away from the guidance path are concentrated in areas where the angle of the guidance path varies significantly, and all distances fall within the pre-set trigger radius of R_{tp} . This indicates that the UAVs will navigate within a narrow, strip-like channel centered on the guidance path, which has a total width of R_{tp} .

The AMD and AVIR of UAV formations of different sizes in the three scenarios are shown in Table 4. In all scenarios, the UAV formation with a straight guidance path is the most tightly structured, slightly higher than the other types of guidance paths,

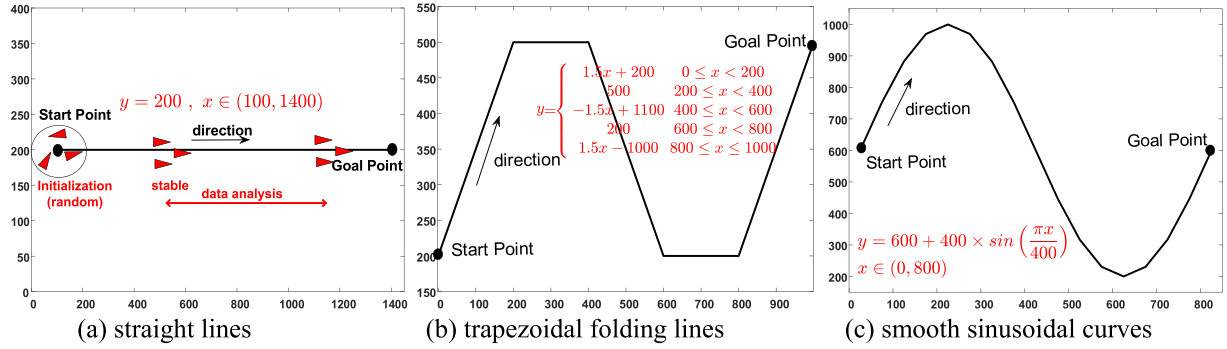


Fig. 7. Schematic of the three guide paths used in Experiment 1.

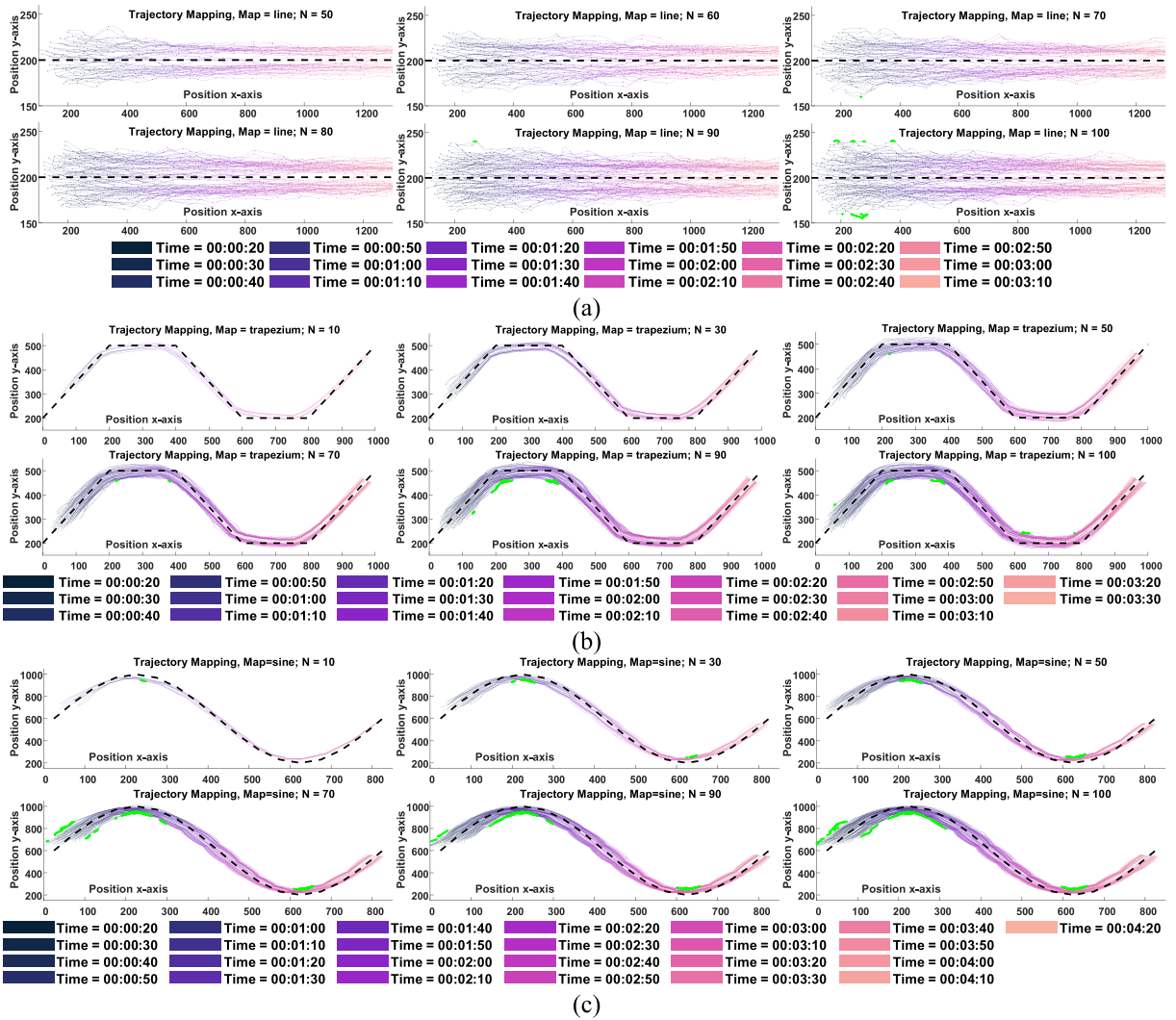


Fig. 8. Trajectory projections in three guide path.

suggesting that the presence of corners in the guidance path slightly reduces the degree of tightness of the UAV formation structure. However, the difference is not significant. For the 10 formation size scenarios, the AMD value difference is 12 %, 13 %, 19 %, 18 %, 19 %, 23 %, 21 %, 23 %, 24 %, and 21 %. In Table 4, the expansion of UAV formation size reduces the AMD, making the formation structure tighter, thus leading to a slight decrease in the formation's mission execution efficiency. Formations have instead lower AVIR

Table 4

Statistical results of AMD and AVIR in Experiment 1.

angle	indicator	$N = 10$	$N = 20$	$N = 30$	$N = 40$	$N = 50$	$N = 60$	$N = 70$	$N = 80$	$N = 90$	$N = 100$
0°	AMD (m)	33.01	20.86	16.67	14.18	12.84	11.74	10.99	10.11	9.62	9.22
60°		33.38	21.01	16.77	14.40	13.21	12.04	11.12	10.36	9.81	9.36
180°		33.42	23.51	19.86	16.70	15.26	14.40	13.29	12.48	11.89	11.18
0°	AVIR	0.0875	0.1214	0.1376	0.1493	0.1570	0.1626	0.1674	0.1709	0.1753	0.1799
60°		0.0891	0.1234	0.1384	0.1510	0.1600	0.1675	0.1736	0.1792	0.1824	0.1870
180°		0.0786	0.1113	0.1285	0.1402	0.1487	0.1549	0.1616	0.1675	0.1725	0.1758

in smooth sinusoidal curves scenarios with higher AMD, demonstrating a higher mission execution efficiency.

Fig. 9 shows the statistical comparison results of the UAV runtime and the number of UAV collisions in 30 repetitions of the experiment for all scenarios. In the scenario of linear guidance path, no collision occurred for all formation sizes under a large number of repetitions of the test. In the scenario of trapezoidal folded guidance path, only a few UAV collisions occurred in the scenario of formation size of 100. In the sinusoidal guidance path scenario, the formation collided in six sets of these repeated experiments, with a maximum of 22 collisions occurring at formation $N = 70$ and $N = 90$. The number of collisions in the current simulation scenarios and experimental parameter settings represents a tiny percentage of the overall running time. Therefore, when using this system, it is essential to adjust the relevant parameters of the formation control system based on the mission's importance, the value of each UAV, and other practical considerations. This will help balance the various practical needs effectively.

3.1.2. Experiment 2: formation convergence speed

Experiment 2 aims to investigate the time required for UAV formations of different sizes to achieve stable flight. Specifically, we will examine the variation in statistical results related to the pre-formation control period for these UAV formations. This investigation is conducted in the context of the first scenario established in Experiment 1, where the steering path is a straight line. Fig. 10 gives the AMD, AVCR, and AVIR changes of the UAV formation in the first 200 s of the scenario, respectively, and zooms in on some of the images. According to Fig. 10, the change trends of the AMD, AVCR, and AVIR of formations of different sizes are almost the same. All of them can reach a stable state at a time node of no >5 s, which indicates that the convergence speed of the formation control system proposed in this paper is less affected by the size of the formations. The FCS can reach a stable state in a very short period.

In Fig. 8, the trajectory projection's width gradually decreases with the operation of the formation. In contrast, in Fig. 10(a), the average shortest path of the UAV formation gradually increases with the operation of the formation. So Fig. 11 gives the positions of the individual UAVs in the formation at the four-time nodes in this scenario when the formation size is $N = 100$, where the transparency of the UAV's outer envelope sphere denotes the speed magnitude of the current UAV, and the higher the speed, the lower the transparency. We adopt the initial position of randomization and the initial method of maximum speed and maximum acceleration in this paper. Therefore, in the early stage of the formation operation, the high-speed individuals and low-speed individuals are randomly distributed in each position of the formation, and the edges of the formation show a spherical shape. With the operation of the formation, the position of high-speed individuals is in front of the formation, and the position of low-speed individuals is in back of the formation, and the formation shows long stripes, and the density of UAVs per unit area decreases. So the formation presents a situation in which the trajectory width is getting narrower, and the average shortest is getting more low during the operation.

3.2. Flexibility and robustness

3.2.1. Experiment 3: security of encounters between formations

When UAV formations are on a mission, they must maintain their current formation while flying safely and at high speed toward

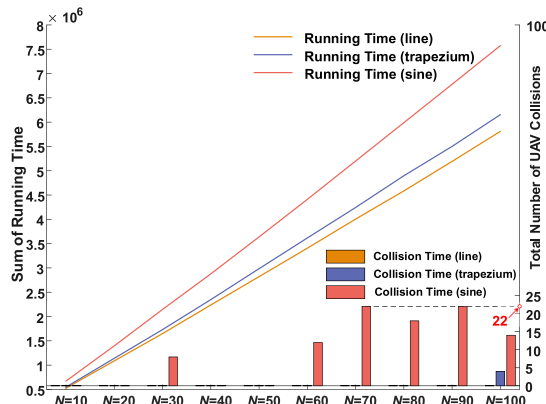


Fig. 9. Statistical results of relevant data in Experiment 1.

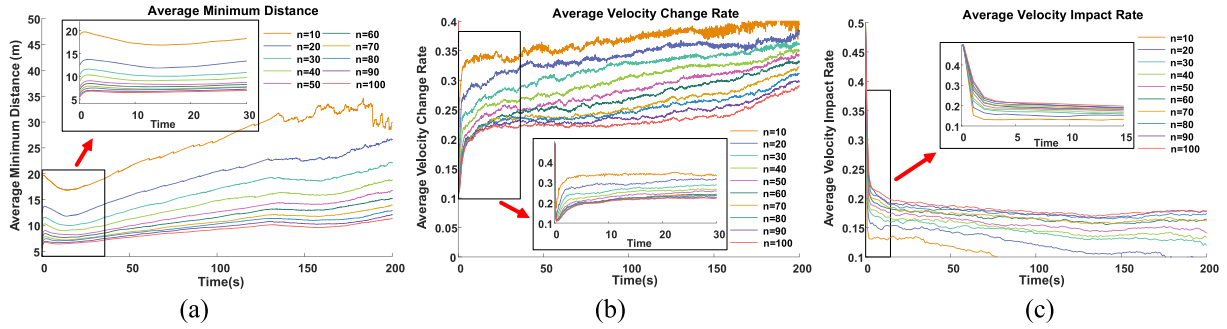


Fig. 10. Statistical results of relevant data in Experiment 2.

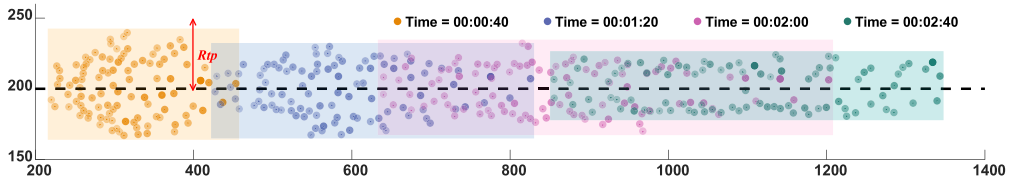


Fig. 11. Schematic of changes in the distribution of UAVs.

the objective point. Avoiding mass formation disruptions or collisions is essential, especially when encountering other formations. Experiment 3 simulates a scenario where two formations meet at various altitudes in the sky. This experiment evaluates the FCS's obstacle avoidance capability by measuring the cluster confusion level when different-sized formations intersect at various angles. Additionally, it assesses the impact on mission progress and the number of dangerous behaviours or collisions that occur. In Experiment 3, two UAV formations fly along different routes based on the guided paths, and two formations meet in the middle period of the routes at 0° , 60° , 90° , 120° and 180° .

Fig. 12 gives the positional trajectory projections of UAV formations of different sizes for the period of formation encounters at different angles, where the red or blue dashed lines are the guided paths of the different formations. Based on Fig. 12, the formation can reasonably plan the operation trajectory during the encounter, and a smaller size of the formation of a smaller angle of the encounter between the formations reduces the confusion of the formations during the encounter.

By observing scenario 90° and scenario 120° , the UAV formations tend to fly towards the average flying angle of the two formations first in the encounter, separate from the other formations at the appropriate time nodes, and return to their belonging formation.

Table 5 gives the statistical results of the AMD (m), ART (per 1 km), AVCR, AVIR, AWR, and AESR for different sizes of UAV formations in different scenarios under the control of the FCS, respectively.

According to Table 5 (regarding the AMD and ART), the AMD of the UAV formations in scenarios 60° and 120° is smaller than their AMD in scenarios 90° and scenarios 180° . As the UAV formation size increases, the AMD decreases in all scenarios. In that experiment, there was a 1000 % difference between the maximum and minimum values of formation size. However, across the five scenarios, The AMD only declined by 64 %, 71 %, 69 %, 73 % and 68 %, and ART increased by 10 %, 13 %, 14 %, 14 % and 12 %. The AMD in all scenarios is much larger than the R_e set in this paper, suggesting that the FCS will balance the structural tightness and safety of the formation based on the UAV formation size. Based on Table 5(ART and AVIR), the ART and AVIR of the UAV formation in scenarios 60° and 120° are both smaller than their corresponding values in scenarios 90° and 180° , so to reduce the interactions between the formations and to improve the efficiency of the task execution of the formations, the intersecting of the guidance paths into a vertical or relative direction should be avoided during the task initialization process. When comparing Table 5 (regarding the APT and AVCR), it becomes evident that as the formation size increases, the ART also increases across all scenarios. In contrast, the AVCR decreases. This indicates that the formation experiences a short-lived low-movement-speed state upon encountering others, and the duration of this state lengthens with larger formation sizes. Therefore, to enhance mission execution efficiency, the large-scale formation should avoid meeting at the same moment during the mission setup. Table 5(regarding the AWR and AESR) shows the AWR and AESR of different sizes of UAV formations in different scenarios; according to Table 5(regarding the AWR), the formation triggers the escape system regardless of UAV sizes, and the angle at which the formation meets and the formation's AWR is higher when the guided paths are vertically oriented or intersecting in relative directions, and AWR also increases with the increase of formation size. When comparing Table 5 (specifically the AMD and AWR), except for scenario 0° , the AWR increases as the AMD increases. Therefore, when initializing the guidance paths, it is advisable to keep the different formation guidance paths aligned as closely as possible at the point of intersection to enhance the safety of the formations. In Table 5 (regarding the AESR), we note that the AESR in scenario 0° remains at 100 % throughout the operation of both UAV formations, each consisting of 50 units. This indicates that with the current parameter settings and simulated environments, even UAV formations with a size of 100 can achieve extremely high safety levels. Additionally, the Average Escape Success Rate of the formation is significantly lower in scenario 180° compared to the other scenarios. To improve

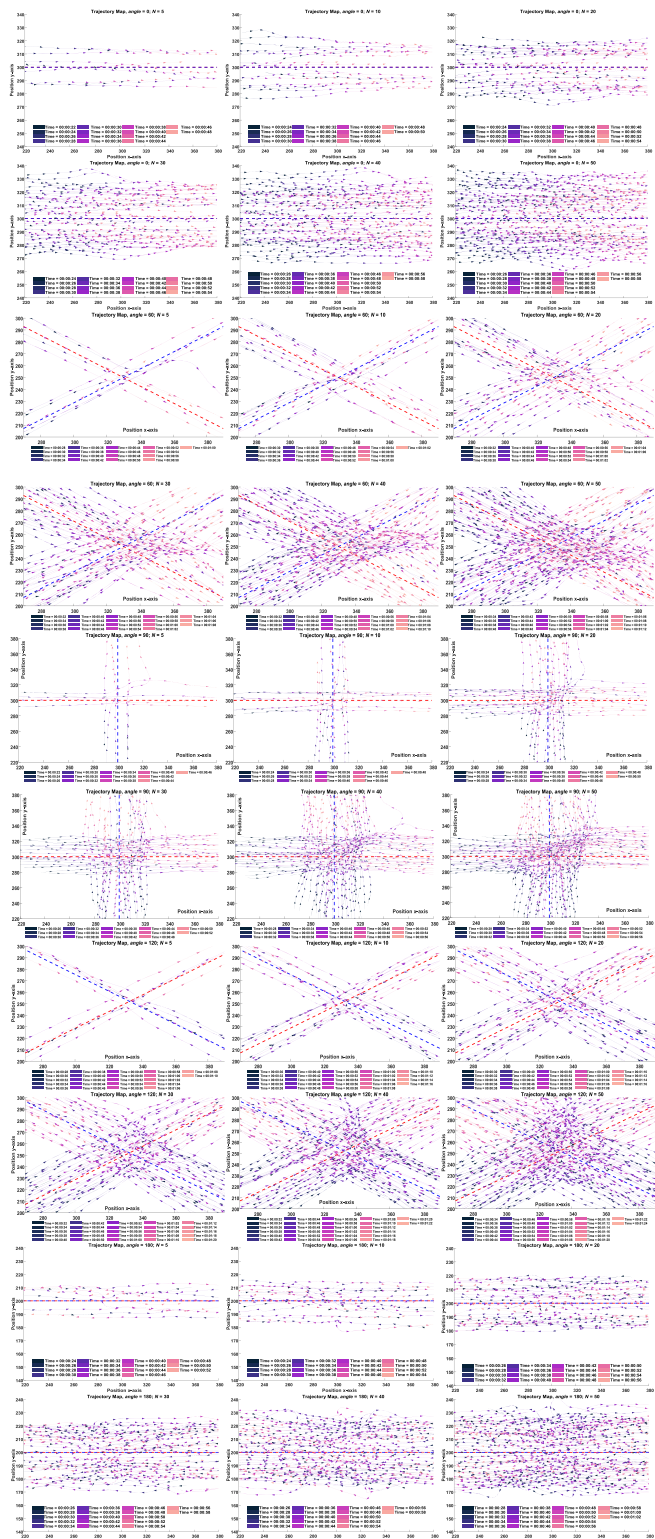


Fig. 12. Trajectory projections of two formations in different encounter scenarios.

Table 5

Statistical results of formation-related data under different encounter scenarios.

angle	indicator	N = 5	N = 10	N = 20	N = 30	N = 40	N = 50	indicator	N = 5	N = 10	N = 20	N = 30	N = 40	N = 50
0°	AMD (m)	20.48	14.18	10.21	8.72	7.84	7.31	AVIR	0.1249	0.1475	0.1673	0.1788	0.1857	0.1929
		33.94	21.77	15.15	12.45	10.74	9.81		0.0842	0.1143	0.1421	0.1591	0.1721	0.1839
		28.18	19.05	13.21	10.84	9.64	8.70		0.0976	0.1251	0.1519	0.1697	0.1840	0.1960
		35.29	21.80	14.96	12.46	10.64	9.67		0.0819	0.1175	0.1434	0.1602	0.1741	0.1851
		26.70	18.20	12.76	10.50	9.20	8.47		0.1086	0.1351	0.1618	0.1780	0.1903	0.2007
	ART (/1 km)	140.6	144.4	148.6	151.4	153.5	155.2	AWR	0.0000	0.0000	0.0001	0.0005	0.0015	0.0023
		134.8	139.1	143.6	146.5	149.2	151.9		0.0001	0.0004	0.0010	0.0024	0.0037	0.0056
		136.5	139.9	146.4	148.9	153.5	155.9		0.0006	0.0013	0.0035	0.0064	0.0096	0.0148
		133.6	139.8	142.5	146.5	149.2	151.6		0.0005	0.0009	0.0023	0.0039	0.0057	0.0083
		139.8	143.5	147.6	150.5	153.8	156.6		0.0039	0.0062	0.0095	0.0118	0.0155	0.0182
0°	AVCR	0.3185	0.2904	0.2521	0.2385	0.2276	0.2229	AESR	1.0000	1.0000	1.0000	1.0000	1.0000	1.0000
		0.3706	0.3437	0.3070	0.2792	0.2554	0.2415		1.0000	1.0000	0.9947	0.9990	0.9972	0.9982
		0.3522	0.3290	0.2908	0.2579	0.2417	0.2239		1.0000	1.0000	0.9984	0.9924	0.9919	0.9921
		0.3671	0.3386	0.3042	0.2763	0.2561	0.2382		1.0000	0.9879	0.9790	0.9840	0.9861	0.9846
		0.3423	0.3156	0.2700	0.2430	0.2219	0.2128		0.9415	0.9530	0.9573	0.9604	0.9602	0.9651

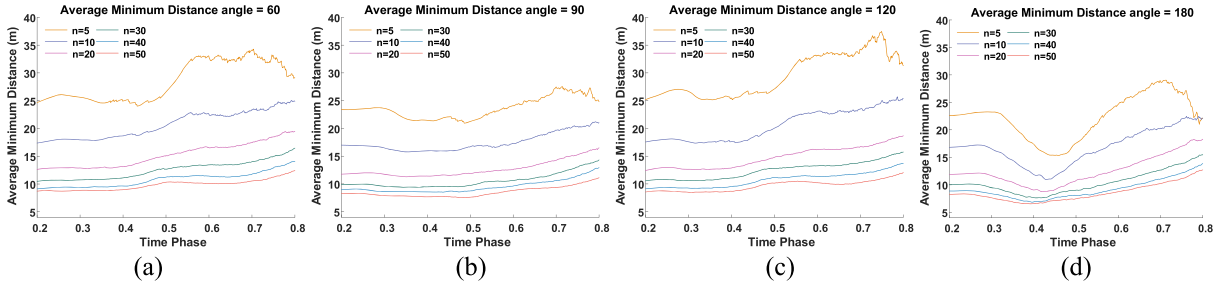


Fig. 13. The AMD in different scenarios.

safety in other scenarios, appropriately increasing the Re , Rs and ω_s is necessary.

Fig. 13 shows the changing trends of the AMD at 60° , 90° , 120° , 180° with respect to the time phase. The time phase is defined as the ratio of the current run time to the maximum run time of the current formation. Under this definition, the formations in all the scenarios intersect at approximately a time phase of 0.5. Since the FCS only provides flight instructions for the navigation phase of the formation, only the trend graphs between 0.2 and 0.8 were provided.

Fig. 13 shows that the AMD of the scenarios other than the scenario 180° undergoes a relatively obvious hardly change during the formation operation. This illustrates the FCS can maintain its own structural tightness even in the event of UAV formation encounters.

Fig. 14 provides the variation curves of AWR (solid line) and ACR (shaded area) with time phases at 0° , 60° , 90° , 120° , 180° . Since the FCS only provides flight instructions for the navigation phase of the formation, only the trend graphs between 0.2 and 0.8 were provided. According to Fig. 14, most of the high AWR of the UAVs in the formation is concentrated in the formation encounter period, and the AWR lines under different formation size conditions show a similar trend. For the same formation size, although the AWR for part period in scenario 120° is significantly higher than the corresponding value in scenario 180° , the ACR for this time period is significantly lower than the corresponding value in scenario 180° , which suggests that the angle of formation encounters plays an important role in the safety of FCS.

3.2.2. Experiment 4: formation separation and combination

In Experiment 4, we focused on the ability of formations to separate into multiple formations and the ability of multiple formations to combine into a single formation during mission execution. We designed a test environment centred around a hexagon with three mission start points and three mission target points to investigate this. Three independent UAV formations began their missions at the three start points and performed three separations and combinations while navigating through the vertices of the hexagon. The test environment is illustrated schematically in Fig. 15. At the left separation point, the formation splits into two formations with equal probability. The other separation points split with a probability of 33.33 % toward mission target point 2.

The projections of the trajectories of three UAV formations with formation sizes of 10, 20, 30, 40, and 50 in the test environment are shown in Fig. 16. In all the experiments of formation separation and combination, there were no collisions between UAVs.

The number of times the formation triggered the escape system in 30 repetitions of the experiment is given in Fig. 17 with its corresponding time phase. In Fig. 17, the time phases for triggering the escape strategy are concentrated in the two parts with time phases of 0.2 and 0.5, reflecting that the formation will have a particular impact on the formation structure when separating and combining. However, it will not impact the safety of the UAV formation. According to Figs. 16 and 17, the FCS can stably and safely process the separation and combination commands of different sizes of formations, and the formation can change its structure flexibly.

3.2.3. Experiment 5: formation encountered signal interference

During flight mission execution, the formation is affected by airflow, signal interference, sensor error, and other factors, and some

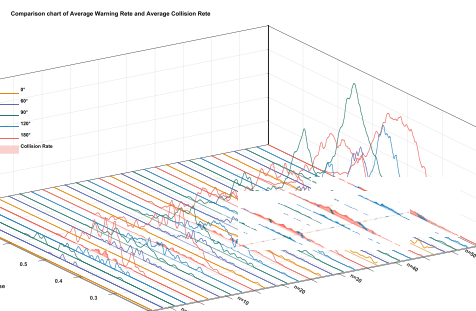


Fig. 14. AWR and ACR in different scenarios.

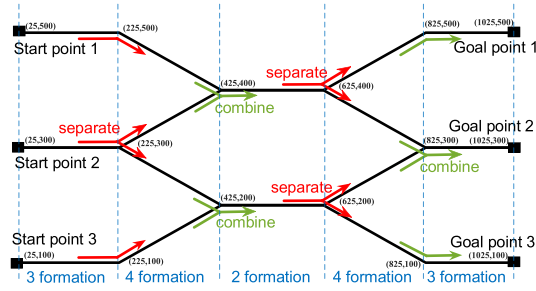


Fig. 15. Schematic of experimental map in Experiment 4.

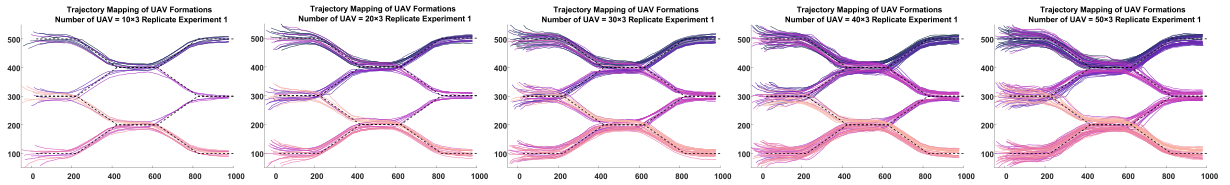


Fig. 16. UAV projection trajectories for Experiment 4.

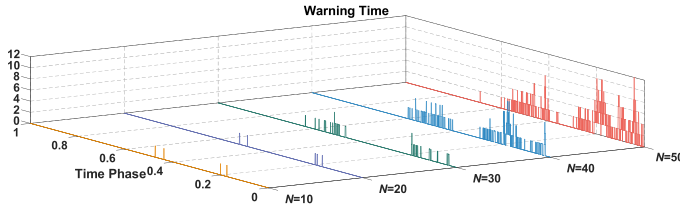


Fig. 17. Statistical results of formation warning time in Experiment 4.

differences may exist between the flight instructions and the actual flight state, thus reducing the safety of the formation flight process. In Experiment 5, we added different ranges of noise signal interference (SI) to the flight instructions to generate errors between the flight instructions and the actual flight state and recorded, compared, and analyzed the differences between the performance indexes of the formation to test the robustness of the FCS.

In this experiment, the frequency of the noise disturbance is 10hz, which is randomly generated and uniformly distributed with the flight command. The maximum values are 5 %, 10 % and 15 % of the maximum flight speed, respectively. Additionally, in the process of formation flight, due to the change in UAV model performance or the adjustment of the mission control center, the fuselage parameters of the UAV may also change, so a set of comparative experiments in which the fuselage parameters are randomly changed according to a specific frequency within a certain range are added to the simulation experiment, which is also used to test the robustness of the formation control system.

The length of the preset guidance path was firstly unified in this experiment, and the test environment was set up as a circular track with r as the center of the circle, a radius length of 100, and a length of 628 m. The test environment was set up as a circular track with [150, 150] as the circle's center and a radius length of 100. The UAV formation flew along the circular guidance path in a clockwise cycle. New UAVs joining the formation were uniformly generated in a particular range on the outside of the track. Since the FCS only provides flight instructions for the navigation phase of the formation. During the initialization phase, we randomly assign formation individuals around the starting point, provide them with a random initial velocity, and then intercept the stable flight process after a while (entering the circular track) for data analysis. A schematic of the experimental scenario for Experiment 5 is shown in Fig. 18. Where the blue dotted line indicates the guided path. The UAV is guided into the circular track area by a guided path pointing from the far end into the data analysis area after initialisation outside the area.

Table 6 presents the statistical results of the average AMD, AVIR, and AWR of UAV formations affected by noise signals of various sizes during operation, in both the parameter-fixed (PF) and parameter-updated (PU) scenarios. According to Table 6, the AMD of the formation increases in the case of the formation subjected to two kinds of perturbations, indicating that the compactness of the formation decreases at this time. The AWR of the formation decreases as the compactness of the formation decreases, indicating improved safety of the airframe when facing perturbations. When there is a discrepancy between the formation's flight instructions and its actual flight state, the overall flight speed of the formation decreases; however, this reduction is <2 % of the maximum flight speed, resulting in only a minor impact on mission execution efficiency. During parameter updates, the formation's AVIR decreases, but this indicates

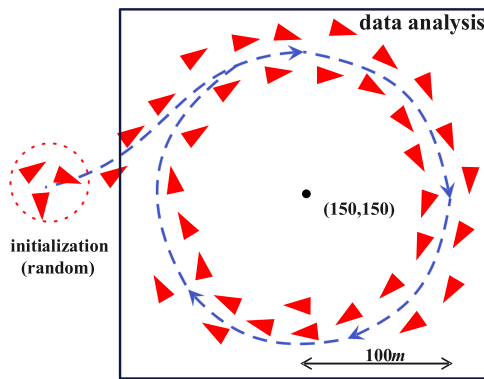


Fig. 18. Schematic diagram of the experimental scenario for Experiment 5.

Table 6

Statistical results of AMD AWR and AVIR in Experiment 5.

SI	AMD (m)		AWR		AVIR	
	PF	PU	PF	PU	PF	PU
0	9.68	9.74	0.0832	0.0531	0.2287	0.2249
0.05	9.65	9.76	0.0847	0.0490	0.2299	0.2268
0.10	9.72	9.86	0.0826	0.0352	0.2356	0.2320
0.15	9.83	9.99	0.0654	0.0367	0.2429	0.2399

an actual improvement in mission execution efficiency at that time. Therefore, the FCS demonstrates significant robustness. Although modifying UAV parameters reduces the compactness of the formation, it simultaneously enhances both safety and mission execution efficiency. This suggests that the FCS supports more frequent parameter modifications for the UAVs in the formation, leading to increased flexibility in mission execution.

3.3. Ablation experiment

The global interaction component of the formation plays the central control role during the mission execution. In Ablation experiment, this paper verifies the reasonableness of the design of each component of the FCS by removing the other components of the FCS in turn. The experimental scenarios and related parameter settings of this paper are the same as those of Experiment 5, and the systems that are compared with the original FCS proposed in this paper are FCS without linear separation effect, FCS without escape system, and FCS without local interaction. The statistical results of AMD, AVIR, and AWR for 30 repetitions of the experiment are given in [Table 7](#).

According to [Table 7](#), the AMD were 33.9 % and 33.8 % of the FCS without linear separation effect for the original FCS and FCS without escape systems, respectively. The AVIR were 49.0 % and 48.9 %, respectively. So the original FCS and FCS without escape systems have similar tight formation structures and more efficient task execution. However, the FCS without escape systems has higher AWR and less safety of the formation. Compared to the Original FCS, although FCS without linear separation effect and FCS without local interaction have lower AWR, their safety is based on higher AMD, i.e., its formation structure is loose and less practical.

[Fig. 19](#) illustrates the projection of the formation run trajectories of the Original FCS, FCS without linear separation effect, FCS without escape system, and FCS without local interaction over part of the period in the first replicate experiment. In [Fig. 19](#), the formation trajectories of the Original FCS and FCS without an escape system are almost the same, which are stable and almost unaffected by the formation size during the whole operation. FCS without local interaction can maintain the stability of operation when the formation size is small, but with the increase of formation size, some UAVs show the fluctuation of trajectory. The larger the formation size, the more serious the fluctuation phenomenon, i.e., the stability of the system of FCS without local interaction is easily affected by the formation size. The FCS without a linear separation effect system makes it almost difficult to control the UAV swarm to

Table 7

Statistical results of indicators related to different FCSs in ablation experiments.

Algorithm name	AMD (m)	AVIR (%)	AWR (%)
Original FCS	9.6606	22.88	8.60
FCS without linear separation effect	28.5178	46.69	0.08
FCS without escape system	9.6352	22.82	38.81
FCS without local interaction	11.5140	24.94	0.43

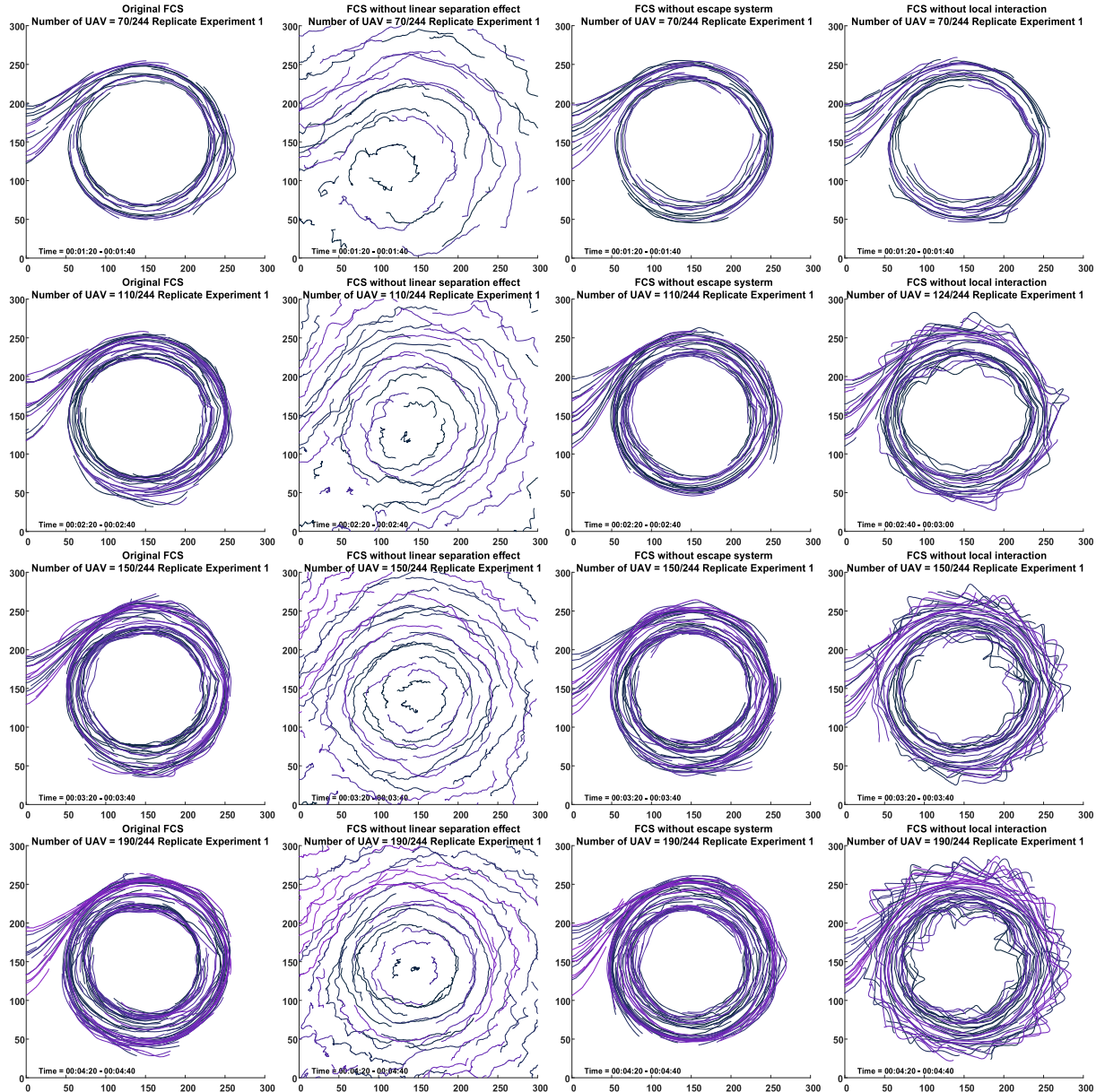


Fig. 19. Trajectory projections of different FCS in Ablation experiment.

produce formation behavior, and the trajectory fluctuation of UAVs is so significant that it has almost no practical value, so this paper does not make further analysis.

4. Conclusion

This paper presents a distributed large-scale joint non-uniform UAV formation real-time path planning system. It introduces a behavior-based formation coordination control method utilizing the GPP technique. This method ensures that the path planning process meets real-time requirements and enhances the success rate of task execution while effectively avoiding the limitations of the LPP method, which relies solely on local environmental information and can lead to stagnation. We enhance the safety and stability of the formation control system by designing the FCM components incorporating a local interaction component, a linear separation force strategy, and an escape system, which serves as an active fault-tolerance control strategy. Although some components have a modest impact on the control command generation process, ablation experiments have confirmed their importance: removing any of these components will reduce the FCS's performance.

While the FCS demonstrates advantages in real-time stability and scalability, we identified several issues during our experiment:

- (1) The behavior-based coordination control method used in the formation poses a risk of collision among agents. This risk arises from inadequate environmental information acquisition, but we can reduce the likelihood of collisions by increasing the safety distance. However, this approach compromises the tightness of the formation, thereby decreasing the overall efficiency of task execution. We plan to integrate hazard prediction systems and visual attention models into the FCS to address this. These enhancements will allow agents to better assess their surroundings and current motion states.
- (2) Although FCS can scale effectively, the current method does not account for network bandwidth limitations encountered in real-world applications. Additionally, local network signal transmission can be delayed, hindering high-frequency local information exchange. Moving forward, we will revise the FCS frameSwork to incorporate multi-level agent leaders for the formation. This adjustment will reduce local networks' dependency and facilitate better control of the joint non-uniform UAV formation.

We will also expand the FCS to include a three-dimensional planning space and implement a suitable flight altitude adjustment strategy within it. Although UAVs cannot make frequent altitude adjustments, incorporating low-frequency altitude adjustment strategies into the FCS can significantly enhance its safety and stability while only requiring a minor sacrifice in range. In the future, we hope that the path planning algorithm we designed can be applied to real formation control systems to detect the performance gap between our algorithm and other traditional algorithms in a real environment.

Availability of data and materials

All data generated or analysed during this study are included in this published article.

CRediT authorship contribution statement

Gang Hu: Writing – review & editing, Writing – original draft, Supervision, Resources, Project administration, Methodology, Investigation, Funding acquisition, Formal analysis, Data curation, Conceptualization. **Peidong He:** Writing – review & editing, Writing – original draft, Visualization, Validation, Software, Methodology, Investigation, Formal analysis, Data curation. **Guo Wei:** Writing – review & editing, Writing – original draft, Supervision, Software, Resources, Methodology, Investigation, Formal analysis, Conceptualization.

Declaration of competing interest

The authors declare that they have no known competing financial interests or personal relationships that could have appeared to influence the work reported in this paper.

Acknowledgments

This work is supported by the National Natural Science Foundation of China (Grant No 52375264).

Supplementary materials

Supplementary material associated with this article can be found, in the online version, at [doi:10.1016/j.apm.2025.116239](https://doi.org/10.1016/j.apm.2025.116239).

Data availability

Data will be made available on request.

References

- [1] W. Wang, UAV formation path planning for mountainous forest terrain utilizing an artificial rabbit optimizer incorporating reinforcement learning and thermal conduction search strategies, *Adv. Eng. Inf.* (2024), <https://doi.org/10.1016/j.aei.2024.102947>.
- [2] S. Aggarwal, N. Kumar, Path planning techniques for unmanned aerial vehicles: a review, solutions, and challenges, *Comput. Commun.* 149 (2020) 270–299, <https://doi.org/10.1016/j.comcom.2019.10.014>.
- [3] M.A. Sadi, A. Jamali, A.M.N.B.A. Kamaruddin, V.Y.S. Jun, Cascade model predictive control for enhancing UAV quadcopter stability and energy efficiency in wind turbulent mangrove forest environment, *E-Prime - Advances in Electrical engineering*, *Electron. Energy* 10 (2024) 100836, <https://doi.org/10.1016/j.prime.2024.100836>.
- [4] H. Wen, Route planning for UAVs maritime search and rescue considering the targets moving situation, *Ocean Eng.* (2024), <https://doi.org/10.1016/j.oceaneng.2024.118623>.
- [5] Z. Xu, Research on precise route control of unmanned aerial vehicles based on physical simulation systems, *Results. Phys.* (2024).
- [6] R. Zhou, T. Tjahjadi, Colour guided ground-to-UAV fire segmentation, *ISPRS Open J. Photogr. Remote Sens.* 14 (2024) 100076, <https://doi.org/10.1016/j.phphoto.2024.100076>.
- [7] G. Chen, Estimating water quality parameters of freshwater aquaculture ponds using UAV-based multispectral images, *Agric. Water. Manage* (2024), <https://doi.org/10.1016/j.agwat.2024.109088>.

- [8] W. Chen, Microtopography-guided precision restoration of sandy lands through UAV: a case study in Hunshandake Sandy Land, China, (2024). <https://doi.org/10.1016/j.catena.2024.108489>.
- [9] R. Yamashita, Sustainable paddy farming in rural Japan: leveraging farmer integration and agricultural UAVs for synergistic solutions, *J. Clean. Prod.* (2024), <https://doi.org/10.1016/j.jclepro.2024.143685>.
- [10] A. Gohari, A.B. Ahmad, K. Mokhtar, T.S.B. Abd Manan, O.O. Oluwatosin, MohammedS.M. Gismalla, A.S. Ab Latip, A. Rostami, A.T. Sholagberu, M.H. Nahi, Systematic review of UAV-assisted airborne particulate matter measurement in urban areas, *Remote Sens. Appl. Soc. Environ.* 36 (2024) 101368, <https://doi.org/10.1016/j.rssae.2024.101368>.
- [11] P. Aela, H.-L. Chi, A. Fares, T. Zayed, M. Kim, UAV-based studies in railway infrastructure monitoring, *Autom. Constr.* 167 (2024) 105714, <https://doi.org/10.1016/j.autcon.2024.105714>.
- [12] Y. Zhu, Y. Yan, A. Dai, H. Dai, Y. Zhang, W. Zhang, Z. Wang, J. Li, UAV-MSSH: a novel UAV photogrammetry-based framework for mining surface three-dimensional movement basin monitoring, *Measurement* 242 (2025) 115944, <https://doi.org/10.1016/j.measurement.2024.115944>.
- [13] Y. Zhi, L. Liu, B. Guan, B. Wang, Z. Cheng, H. Fan, Distributed robust adaptive formation control of fixed-wing UAVs with unknown uncertainties and disturbances, *Aerosp. Sci. Technol.* 126 (2022) 107600, <https://doi.org/10.1016/j.ast.2022.107600>.
- [14] M. Chen, B. Li, J. Wang, G. Wang, A formation control algorithm for Air-Ground Cooperative UAV, in: 2022 14th International Conference on Wireless Communications and Signal Processing (WCSP), IEEE, Nanjing, China, 2022, pp. 741–747, <https://doi.org/10.1109/WCSP5476.2022.10039110>.
- [15] D. Zhang, H. Duan, Variational resolution probability maps for multi-UAV search tasks with changeable searching behaviors, *Aerosp. Sci. Technol.* 155 (2024) 109669, <https://doi.org/10.1016/j.ast.2024.109669>.
- [16] R. Wang, M. Lungu, Z. Zhou, X. Zhu, Y. Ding, Q. Zhao, Least global position information based control of fixed-wing UAVs formation flight: flight tests and experimental validation, *Aerosp. Sci. Technol.* 140 (2023) 108473, <https://doi.org/10.1016/j.ast.2023.108473>.
- [17] J. Xu, Invulnerability optimization of UAV formation based on super wires adding strategy, (n.d.).
- [18] L. Wang, A survey of underwater search for multi-target using Multi-AUV: task allocation, path planning, and formation control, *Ocean Eng.* (2023).
- [19] J. Chen, T. Li, Y. Zhang, T. You, Y. Lu, P. Tiwari, Global-and-local attention-based reinforcement learning for cooperative behaviour control of multiple UAVs, (n.d.).
- [20] J. Chen, Y. Zhang, L. Wu, T. You, X. Ning, An adaptive clustering-based algorithm for automatic path planning of heterogeneous UAVs, *IEEE Trans. Intell. Transport. Syst.* 23 (2022) 16842–16853, <https://doi.org/10.1109/TITS.2021.3131473>.
- [21] J. Chen, Y. Wang, Y. Zhang, Y. Lu, Q. Shu, Y. Hu, Extrinsic-and-intrinsic reward-based multi-agent reinforcement learning for multi-UAV cooperative target encirclement, (n.d.).
- [22] D. Zheng, UAVs cooperative task assignment and trajectory optimization with safety and time constraints, (2023).
- [23] C. Zhang, A dynamic parameters genetic algorithm for collaborative strike task allocation of unmanned aerial vehicle clusters towards heterogeneous targets, (2025).
- [24] Y.V. Pehlivanoglu, P. Pehlivanoglu, An enhanced genetic algorithm for path planning of autonomous UAV in target coverage problems, *Appl. Soft. Comput.* 112 (2021) 107796, <https://doi.org/10.1016/j.asoc.2021.107796>.
- [25] X. Yu, N. Jiang, X. Wang, M. Li, A hybrid algorithm based on grey wolf optimizer and differential evolution for UAV path planning, *Expert. Syst. Appl.* 215 (2023) 119327, <https://doi.org/10.1016/j.eswa.2022.119327>.
- [26] H. Li, T. Zhao, S. Dian, Forward search optimization and subgoal-based hybrid path planning to shorten and smooth global path for mobile robots, *Knowl. Based Syst.* 258 (2022) 110034, <https://doi.org/10.1016/j.knosys.2022.110034>.
- [27] J. Yu, M. Yang, Z. Zhao, X. Wang, Y. Bai, J. Wu, J. Xu, Path planning of unmanned surface vessel in an unknown environment based on improved D*Lite algorithm, *Ocean Eng.* 266 (2022) 112873, <https://doi.org/10.1016/j.oceaneng.2022.112873>.
- [28] M. Yao, H. Deng, X. Feng, P. Li, Y. Li, H. Liu, Improved dynamic windows approach based on energy consumption management and fuzzy logic control for local path planning of mobile robots, *Comput. Ind. Eng.* 187 (2024) 109767, <https://doi.org/10.1016/j.cie.2023.109767>.
- [29] R. Sarkar, D. Barman, N. Chowdhury, Domain knowledge based genetic algorithms for mobile robot path planning having single and multiple targets, *J. King Saud Uni. Comput. Inf. Sci.* 34 (2022) 4269–4283, <https://doi.org/10.1016/j.jksuci.2020.10.010>.
- [30] M. Dakulović, S. Horvatić, I. Petrović, Complete coverage D* algorithm for path planning of a floor-cleaning mobile robot, *IFAC Proc. Volumes* 44 (2011) 5950–5955, <https://doi.org/10.3182/20110828-6-IT-1002.03400>.
- [31] M. Dakulović, I. Petrović, Two-way D* algorithm for path planning and replanning, *Rob. Auton. Syst.* 59 (2011) 329–342, <https://doi.org/10.1016/j.robot.2011.02.007>.
- [32] Y. Liu, A passage time-cost optimal a* algorithm for cross-country path planning, *Int. J. Appl. Earth Observ. Geoinf.* (2024).
- [33] L. Yin, Z. Yan, Q. Tian, H. Li, J. Xu, A novel robust algorithm for path planning of multiple autonomous underwater vehicles in the environment with ocean currents, *Ocean Eng.* 312 (2024) 119260, <https://doi.org/10.1016/j.oceaneng.2024.119260>.
- [34] C. Huang, T. Wang, S. Wang, J. Xu, Dynamic path planning for spacecraft rendezvous and approach based on hybrid honey badger algorithm, (n.d.). <https://doi.org/10.1016/j.jfranklin.2024.107398>.
- [35] B. Tu, F. Wang, X. Han, 3D path planning for UAV based on A hybrid algorithm of marine predators algorithm with quasi-oppositional learning and differential evolution, *Egypt. Inf. J.* 28 (2024) 100556, <https://doi.org/10.1016/j.eij.2024.100556>.
- [36] L. Liu, X. Wang, X. Yang, H. Liu, J. Li, P. Wang, Path planning techniques for mobile robots: review and prospect, *Expert. Syst. Appl.* 227 (2023) 120254, <https://doi.org/10.1016/j.eswa.2023.120254>.
- [37] B. Sahu, P. Kumar Das, M.R. Kabat, Multi-robot cooperation and path planning for stick transporting using improved Q-learning and democratic robotics PSO, *J. Comput. Sci.* 60 (2022) 101637, <https://doi.org/10.1016/j.jocs.2022.101637>.
- [38] X. Li, L. Wang, Y. An, Q.-L. Huang, Y.-H. Cui, H.-S. Hu, Dynamic path planning of mobile robots using adaptive dynamic programming, *Expert Syst. Appl.* 235 (2024) 121112, <https://doi.org/10.1016/j.eswa.2023.121112>.
- [39] S. Ganeshan, A hybrid sampling-based RRT* path planning algorithm for autonomous mobile robot navigation, *Expert. Syst. Appl.* (2024), <https://doi.org/10.1016/j.eswa.2024.125206>.
- [40] H. Wang, H. Lai, H. Du, G. Gao, IBPF-RRT*: an improved path planning algorithm with ultra-low number of iterations and stabilized optimal path quality, *J. King Saud Uni. Comput. Inf. Sci.* 36 (2024) 102146, <https://doi.org/10.1016/j.jksuci.2024.102146>.
- [41] H. Huang, Y. Shang, X. Liu, X. Liu, P. Qi, An improved Bi-RRT*-based path planning algorithm with adaptive search strategy assignment mechanism for ultra-low-altitude penetration of fixed-wing aircraft, *Aerosp. Sci. Technol.* (2024) 109363, <https://doi.org/10.1016/j.ast.2024.109363>.
- [42] S. Du, Z. Zhu, X. Wang, H. Han, J. Qiao, Real-time local path planning strategy based on deep distributional reinforcement learning, *Neurocomputing* 599 (2024) 128085, <https://doi.org/10.1016/j.neucom.2024.128085>.
- [43] C. Cheng, Q. Sha, B. He, G. Li, Path planning and obstacle avoidance for AUV: a review, *Ocean Eng.* 235 (2021) 109355, <https://doi.org/10.1016/j.oceaneng.2021.109355>.
- [44] B. Yıldız, M.F. Aslan, A. Durdu, A. Kayabasi, Consensus-based virtual leader tracking swarm algorithm with GDRRT*-PSO for path-planning of multiple-UAVs, *Swarm Evol. Comput.* 88 (2024) 101612, <https://doi.org/10.1016/j.swevo.2024.101612>.
- [45] Y. Wang, Path planning for mobile robots in greenhouse orchards based on improved A* and fuzzy DWA algorithms, *Comput. Electron. Agric.* (2024), <https://doi.org/10.1016/j.compag.2024.109598>.
- [46] M. Faroni, N. Pedrocchi, M. Beschi, Adaptive hybrid local-global sampling for fast informed sampling-based optimal path planning, *Auton. Robot.* 48 (2024) 6, <https://doi.org/10.1007/s10514-024-10157-5>.
- [47] H. Guo, Y. Li, H. Wang, C. Wang, J. Zhang, T. Wang, L. Rong, H. Wang, Z. Wang, Y. Huo, S. Guo, F. Yang, Path planning of greenhouse electric crawler tractor based on the improved A* and DWA algorithms, *Comput. Electron. Agric.* 227 (2024) 109596, <https://doi.org/10.1016/j.compag.2024.109596>.
- [48] W. Meng, Y. Gong, F. Xu, P. Tao, P. Bo, S. Xin, Efficient path planning for AUVs in unmapped marine environments using a hybrid local-global strategy, *Ocean Eng.* 288 (2023) 116227, <https://doi.org/10.1016/j.oceaneng.2023.116227>.

- [49] M. Shankar, G. Sushnigdha, A hybrid path planning approach combining artificial potential field and particle swarm optimization for mobile robot, IFAC-PapersOnLine 55 (2022) 242–247, <https://doi.org/10.1016/j.ifacol.2023.03.041>.
- [50] N. Wang, Dynamics-constrained global-local hybrid path planning of an autonomous surface vehicle, IEEE Trans. Veh. Technol. 69 (2020), <https://doi.org/10.1109/TVT.2020.2991220>.
- [51] Y. Wu, K.H. Low, Discrete space-based route planning for rotary-wing UAV formation in urban environments, ISA Trans. 129 (2022) 243–259, <https://doi.org/10.1016/j.isatra.2021.12.043>.
- [52] J. Choi, M. Jeong, E. Lee, D. Choi, H. Myung, NLOS-avoiding and obstacle-adaptive formation control by sharing obstacle information of a leader UAV in Multi-UAV system, (n.d.). <https://doi.org/10.1109/UR57808.2023.10202465>.
- [53] X. Li, B. Li, P. Zhang, J. Zhang, S. Zhang, Large-scale unmanned aerial vehicle formation maintenance algorithm based on virtual structure, (n.d.). <https://doi.org/10.1109/ISCID.2015.5>.
- [54] H. Wang, Y. Huang, J. Chu, S. Sun, A virtual structure approach to formation control of multi robots with collision avoidance in space station, (n.d.). <https://doi.org/10.23919/CCCS5666.2022.9902358>.
- [55] Z. Gu, B. Song, Y. Fan, X. Chen, Design and verification of UAV formation controller based on leader-follower method, in: 2022 7th International Conference on Automation, Control and Robotics Engineering (CACRE), IEEE, Xi'an, China, 2022, pp. 38–44, <https://doi.org/10.1109/CACRE54574.2022.9834161>.
- [56] X. Li, H. Zhou, UAV formation centralized control method under cooperative flight missions, in: 2023 5th International Conference on Robotics, Intelligent Control and Artificial Intelligence (RICAI), IEEE, Hangzhou, China, 2023, pp. 366–369, <https://doi.org/10.1109/RICAI60863.2023.10489720>.
- [57] L. Bai, Z. Zhao, X. Meng, Y. Wang, Q. Rao, X. Deng, Research on UAV formation Simulation and Evaluation technology, in: 2022 5th International Conference on Intelligent Autonomous Systems (ICoIAS), IEEE, Dalian, China, 2022, pp. 166–171, <https://doi.org/10.1109/ICoIAS56028.2022.9931226>.
- [58] H. Sheng, J. Zhang, Z. Yan, B. Yin, S. Liu, T. Bai, D. Wang, New multi-UAV formation keeping method based on improved artificial potential field, Chin. J. Aeronaut. 36 (2023) 249–270, <https://doi.org/10.1016/j.cja.2023.07.030>.
- [59] J. Espelosín, L. Acosta, D. Alonso, Path planning approach based on flock dynamics of moving particles, Appl. Soft. Comput. 13 (2013) 2159–2170, <https://doi.org/10.1016/j.asoc.2012.12.015>.
- [60] S. Peccoud, S. Xing, T. Yang, R.S. Stansbury, Behavior-based communication-aware formation control in dynamic multi-agent systems for jamming detection and avoidance, in: SoutheastCon 2024, IEEE, Atlanta, GA, USA, 2024, pp. 552–558, <https://doi.org/10.1109/SoutheastCon52093.2024.10500200>.
- [61] D. Strömbom, C. Futterman, An alignment-free explanation for collective predator evasion in moving animal groups, Dynamics. 3 (2023) 793–802, <https://doi.org/10.3390/dynamics3040043>.
- [62] G. Sun, R. Zhou, Z. Ma, Y. Li, R. Groß, Z. Chen, S. Zhao, Mean-shift exploration in shape assembly of robot swarms, Nat. Commun. 14 (2023) 3476, <https://doi.org/10.1038/s41467-023-39251-5>.
- [63] L. Wang, A. Li, F. Di, H. Lu, C. Wang, Distributed two-channel dynamic event-triggered adaptive finite-time fault-tolerant containment control for multi-leader UAV formations, Aerosp. Sci. Technol. 155 (2024) 109678, <https://doi.org/10.1016/j.ast.2024.109678>.
- [64] L. Wei, M. Chen, T. Li, Disturbance-observer-based formation-containment control for UAVs via distributed adaptive event-triggered mechanisms, J. Franklin Inst. B 358 (2021) 5305–5333, <https://doi.org/10.1016/j.jfranklin.2021.04.050>.
- [65] Y. Ren, F. Zhu, W. Liu, Z. Wang, Y. Lin, F. Gao, F. Zhang, Bubble planner: planning high-speed smooth quadrotor trajectories using receding corridors, (n.d.). <https://doi.org/10.1109/IROS47612.2022.9981518>.
- [66] G. Hu, B. Du, K. Chen, G. Wei, Super eagle optimization algorithm based three-dimensional ball security corridor planning method for fixed-wing UAVs, Adv. Eng. Inf. 59 (2024) 102354, <https://doi.org/10.1016/j.aei.2024.102354>.
- [67] F. Gao, L. Wang, B. Zhou, X. Zhou, J. Pan, S. Shen, Teach-repeat-replan: a complete and robust system for aggressive flight in complex environments, IEEE Trans. Robot. 36 (2020), <https://doi.org/10.1109/TRO.2020.2993215>.
- [68] H. Gupta, O.P. Verma, A novel hybrid Coyote-Particle swarm optimization algorithm for three-dimensional constrained trajectory planning of Unmanned aerial Vehicle, Appl. Soft. Comput. 147 (2023) 110776, <https://doi.org/10.1016/j.asoc.2023.110776>.
- [69] S. Liu, M. Watterson, K. Mohta, K. Sun, S. Bhattacharya, C.J. Taylor, V. Kumar, Planning dynamically feasible trajectories for quadrotors using safe flight corridors in 3-D complex environments, IEEE Robot. Autom. Lett. 2 (2017), <https://doi.org/10.1109/LRA.2017.2663526>.
- [70] B. Zhou, F. Gao, L. Wang, C. Liu, S. Shen, Robust and efficient quadrotor trajectory generation for fast autonomous flight, IEEE Robot. Autom. Lett. 4 (2019), <https://doi.org/10.1109/LRA.2019.2927938>.
- [71] Z. Yu, Y. Zhang, B. Jiang, J. Fu, Y. Jin, A review on fault-tolerant cooperative control of multiple unmanned aerial vehicles, Chin. J. Aeronaut. 35 (2022) 1–18, <https://doi.org/10.1016/j.cja.2021.04.022>.
- [72] Z.X. Liu, X. Yu, C. Yuan, Y.M. Zhang, Leader-follower formation control of unmanned aerial vehicles with fault tolerant and collision avoidance capabilities, (n.d.). <https://doi.org/10.1109/ICUAS.2015.7152392>.
- [73] Q. Xu, H. Yang, B. Jiang, D. Zhou, Y. Zhang, Fault tolerant formations control of UAVs subject to permanent and intermittent faults, J. Intell. Robot. Syst. (2014), <https://doi.org/10.1007/s10846-013-9951-2>.
- [74] A. Abdessameud, A. Tayebi, Formation control of VTOL Unmanned Aerial Vehicles with communication delays, Automatica 47 (2011) 2383–2394, <https://doi.org/10.1016/j.automatica.2011.08.042>.
- [75] H. Yang, Synchronization of multiple 3-DOF helicopters under actuator faults and saturations with prescribed performance, ISA Trans (2018), <https://doi.org/10.1016/j.isatra.2018.02.009>.
- [76] X. Ai, Flatness-based finite-time leader-follower formation control of multiple quadrotors with external disturbances, Aerosp. Sci. Technol. (2019).
- [77] D. Liu, H. Liu, F.L. Lewis, K.P. Valavanis, Robust time-varying formation control for tail-sitters in flight mode transitions, 51 (2021).
- [78] D. Liu, H. Liu, J. Xi, Fully distributed adaptive fault-tolerant formation control for octocopters subject to multiple actuator faults, Aerosp. Sci. Technol. 108 (2021) 106366, <https://doi.org/10.1016/j.ast.2020.106366>.
- [79] X. Zhou, X. Wen, Z. Wang, Y. Gao, H. Li, Q. Wang, T. Yang, H. Lu, Y. Cao, C. Xu, F. Gao, Swarm of micro flying robots in the wild, Sci. Robot. 7 (2022) eabm5954, <https://doi.org/10.1126/scirobotics.abm5954>.